

Emission from HCN and CH₃OH in comets

Onsala 20-m observations and radiative transfer modelling

P. Bergman¹, M. S. Lerner¹, A. O. H. Olofsson¹, E. Wirström¹, J. H. Black¹, P. Bjerkeli¹, R. Parra², and K. Torstensson²

¹ Department of Space, Earth and Environment, Chalmers University of Technology, Onsala Space Observatory, 43992 Onsala, Sweden

e-mail: per.bergman@chalmers.se

² European Southern Observatory, Av. Alonso de Cordova 3107, Vitacura, Santiago, Chile

Received ; accepted

ABSTRACT

Aims. The aim of this work is to characterize HCN and CH₃OH emission from recent comets.

Methods. We used the Onsala 20-m telescope to search for millimetre transitions of HCN towards a sample of 11 recent and mostly bright comets in the period December 2016 to November 2019. Also CH₃OH was searched for in two comets. The HCN sample includes the interstellar comet 2I/Borisov. For the short-period comet 46P/Wirtanen we could monitor the variation of HCN emission over a time span of about one month. We performed radiative transfer modelling for the observed molecular emission by also including time-dependent effects due to the outgassing of molecules.

Results. HCN was detected in 6 comets. Two of these are short-period comets and 4 of them are long-period. Six methanol transitions were detected in 46P/Wirtanen, enabling us to determine the gas kinetic temperature. From the observations, we determined the molecular production rates using time-dependent radiative transfer modelling. For 5 comets, we could determine that the HCN mixing ratios lie near 0.1% using contemporary water production rates, $Q_{\text{H}_2\text{O}}$, taken from other studies. This HCN mixing ratio was also found typical in our monitoring observations of 46P/Wirtanen but here we notice deviations, on a daily time scale, up to 0.2% which could indicate short-time changes in the outgassing activity. From our radiative transfer modelling of cometary comae, we found that time-dependent effects on the HCN level populations are of the order 5-15% when $Q_{\text{H}_2\text{O}}$ is around $2 \times 10^{28} \text{ mol s}^{-1}$. The effects may be relatively stronger for comets with lower $Q_{\text{H}_2\text{O}}$. The exact details of the time-dependent effects depend on the amount of neutral and electron collisions, radiative pumping, and molecular parameters such as the spontaneous rate coefficient.

Key words. comets: general – radio lines: general

1. Introduction

Most comets are expected to be remnants from the early times, some 4.5 billion years ago, when the Solar System was formed, and therefore they may contain records of the chemical and physical properties of these times past. Exceptions to this notion are, of course, the recent discoveries of the objects 1I/Oumuamua and 2I/Borisov which are suggested to be interstellar visitors entering our Solar System with strongly hyperbolic, and thus unbound, trajectories. When approaching the Sun to within a few au, comets can start to sublimate molecules and other volatile particles from their surfaces and form what is known as a cometary coma. The study of the composition of cometary comae content can therefore reveal information on the physical conditions and chemistry prevailing when the Solar System was born or similar systems in the solar neighbourhood in case of the interstellar visitors.

The study of the cometary coma molecular content is performed either by remote sensing (mainly by recording spectral signatures over a wide range of wavelengths from radio to the ultraviolet regimes) or by in-situ measurements made by spacecraft like Giotto (1P/Halley) and, more recently, Rosetta (67P/Churyumov-Gerasimenko). As pointed out by Rubin et al. (2019), most abundances of the volatile content, determined by these various means over the last 40 yrs, are reminiscent of those

in the interstellar medium and thus suggest a chemical origin in interstellar, star-forming material. The major gaseous constituent of the neutral inner coma is water molecules which other species relate to. For instance, the next two most abundant species, CO₂ and CO, constitute typically 10-20% of that of water (Mumma & Charnley 2011; Rubin et al. 2019). Further out in the coma, the solar radiation will affect the composition. At 1 au from the Sun, the outgassing water molecules are photo-dissociated into H and OH at a rate of about $(1 - 2) \times 10^{-5} \text{ s}^{-1}$ (Huebner et al. 1992) where the factor of two variation reflects the degree of solar activity. An about 30 times slower water destruction mechanism is the photo-ionization into H₂O⁺. This latter process, together with photo-ionization of OH, previously formed from water, is the main source of electrons in the coma (Rubin et al. 2009). Since water is relatively difficult to spectroscopically observe, several other, indirect, methods have been employed to determine the water production rate. Firstly, the observations of the photo-dissociation product OH can be used as a proxy for water (Despois et al. 1981; Bonev et al. 2006). Secondly, also observations of the remaining H, via Ly- α , can be used as exemplified by the Solar Wind Anisotropies (SWAN) Ly- α camera observations onboard the Solar and Heliospheric Observer (SOHO) spacecraft (eg. Combi et al. 2011). A third indirect method is to use a relatively abundant parent species, like HCN, as an indicator of water – see Mumma & Charnley (2011) for an overview.

Direct observations of the ground state water lines are scarce and are mostly limited to satellites (e.g. Lecacheux et al. 2003; Lis et al. 2013; Biver et al. 2015). Infrared spectroscopy of the ro-vibrational water lines has proven useful to determine the water production rates (Mumma et al. 2003). This latter method, albeit relying on fluorescence pumping models, has the advantage that the excitation conditions can be determined, via a rotation temperature, and consequently provide more accurate production rates (e.g. DiSanti et al. 2016). Lastly, in-situ measurements by spacecraft, via high-resolution mass spectroscopy, provide perhaps the most direct way, although limited to a few comets, to probe the molecular coma content (e.g. Lauter et al. 2020).

The observations presented in this paper are part of an ongoing effort to study comets at mm wavelengths using the Onsala Space Observatory (OSO) 20-meter telescope. This effort was initiated by Wirstrom et al. (2016) who presented HCN(1-0) observations of the long-period comets C/2013 R1 (Lovejoy) and C/2014 Q2 (Lovejoy). We here expand this study with observations of another twelve comets. The observational efforts focus primarily on using HCN(1-0) as an indicator of water but one comet, 46P/Wirtanen, was also observed in methanol. In fact, both these molecules are believed to be released from nucleus ices (Dello Russo et al. 2016). Our comet target sample comprises bright comets with perihelion dates from late 2016 to 2019. The sample includes comets belonging to the Jupiter family as well as the Oort cloud. In addition, we also searched for HCN towards 2I/Borisov. Furthermore, we also investigate possible caveats, in terms of time-dependent radiative transfer effects, that may complicate the interpretation of the observed emission from HCN (as well as from other molecules) in cometary comae.

This paper is structured as follows. In the next section we describe the observations made with the OSO 20-m telescope. In Sect. 3 we present the results and then, in Sect. 4, we outline the radiative transfer analysis made in which we also take into account time-dependent aspects. After discussing our results in Sect. 5, we finally make our conclusions.

2. Observations

All observations presented in this paper were made from late 2016 until late 2019 using the radome-enclosed OSO 20-m antenna equipped with the 3 mm channel of the 3 and 4 mm receiver system (Belitsky et al. 2015). The radome allows us to observe sources near the Sun without thermal distortion of the telescope optics. The rest frequencies of the target lines, see Table 1, were covered by two frequency tunings, one centred near 88 GHz, and the other near 96 GHz. All tunings were performed in the velocity frame of the comet. Coordinates and velocities of all comets were taken from the Horizons system¹ (Giorgini et al. 1996) tabulated at every 1 hr and then interpolated by the observing system. The antenna half-power beam width is 40 arcsec at the HCN frequency and about 37 arcsec for the CH₃OH observations.

The Fast Fourier Transform Spectrometers (FFTSSs) were configured into a wide 4-GHz mode or a narrow 156 MHz mode. In both modes, both linear polarizations are recorded separately. The wide 4-GHz mode is made up of two partly overlapping 2.5 GHz FFTSSs of 32768 channels and was used for the CH₃OH

observations and part of the HCN observations. The wide mode results in a velocity resolution of about 0.25 km s⁻¹. Normally, the narrow 156 MHz setup was used for the HCN observations. The observations were made in frequency switching mode with a frequency throw for the HCN setup of 5 MHz for data taken in 2016-2017 and 7 MHz from 2018 and onwards. When observing CH₃OH, the wide spectrometer setup was employed to cover all lines, see Table 1, and the used frequency throw was larger, 25 MHz, to avoid line confusion.

The weather conditions during our observations varied. In the best conditions the system temperature was around 120 K. Typically the measurements were automatically halted when the system temperature became large, around 800-1200 K. Pointing and focus optimizations, using the SiO 2-1 $\nu = 1$ maser line at 86 GHz towards stars, were performed several times a day. Measurements from 2018 and onwards were done with the new antenna control system, developed by M. Lerner and called BIFROST², which provides an improved and more automated control of remote observations. We have used these capabilities to perform pointings and focussings automatically every three hours and to automatically pause observations when the system temperature has gone above 800 K. We have been using 60 s and 120 s long integrations for individual scans. With the switch to BIFROST we employed observing blocks consisting of fifteen 60-second scans with hot-load calibrations between every fifth scan.

Information on the 12 comets investigated in this study is summarized in Table 2 where the range of observing date, total integration time, heliocentric distance, R_h , and distance to Earth, Δ , variations over the observing dates also have been entered. Also the projected nucleocentric distance (near the center of the date range), d , as subtended by the beam size for HCN(1-0) transition has been listed.

3. Results

The HCN and CH₃OH observations are displayed in Figs. 1-7. The shown spectra have been smoothed to a resolution of 0.3 km s⁻¹ (except the 46P/Wirtanen global average spectrum) and intensities are shown in T_{mb} -scale. The individual scans were first folded before being noise-weighted to form an average. Because of the frequency switching observing mode, a rather high order polynomial was needed to subtract the baseline. The used baseline order was typically from 3 to 7 where the higher orders were used for the observations with larger frequency throws. The channel RMS and integrated line intensities, I_{mb} , have been entered in Table 3. Errors and upper limits are 1σ in this table. The variation of errors and limits among the comets is a combination of system temperature and integration time. The integrated line intensity of HCN($J = 1 \rightarrow 0$) is calculated as a sum of the three hyperfine structure (hfs) line intensities, listed in Table 1, using a box of width 2 km s⁻¹ centered on each hfs line. The 46P/Wirtanen monitoring measurements have been entered in Table 4. Below we give a short introduction and summary of the results for each comet observed:

- C/2016 U1 (NEOWISE). This comet (hereafter U1), discovered in October 2016 by the Near-Earth Object Wide-field Infrared Survey Explorer (NEOWISE), follows a slightly hyperbolic orbit (eccentricity just above 1). At perihelion on 14

¹ HORIZONS is a service of the Solar System Dynamics group at the NASA/Jet Propulsion Laboratory for computing ephemerides of solar-system bodies. The web interface is at <https://ssd.jpl.nasa.gov/horizons.cgi>

² see <https://www.chalmers.se/en/researchinfrastructure/oso/radio-astronomy/20m/Pages/Handbook.aspx> and http://www.ira.inaf.it/eratec/florence/presentations/florens_Lerner.pdf

Table 1. Observed lines

Molecule	Frequency ^(a) (MHz)	Transition	g_u	$E_u^{(b)}$ (K)	$A_{ul}^{(c)}$ (s ⁻¹)
HCN	88630.42	$J_F = 1_1 - 0_1$	3	4.2	2.4×10^{-5}
	88631.85	$J_F = 1_2 - 0_1$	5	4.2	2.4×10^{-5}
	88633.94	$J_F = 1_0 - 0_1$	1	4.2	2.4×10^{-5}
CH ₃ OH	95169.39	$J_K = 8_0 - 7_1 A^+$	17	83.5	4.3×10^{-6}
	95914.31	$J_K = 2_1 - 1_1 A^+$	5	21.4	2.5×10^{-6}
	96739.36	$J_K = 2_{-1} - 1_{-1} E$	5	12.5	2.6×10^{-6}
	96741.37	$J_K = 2_0 - 1_0 A^+$	5	7.0	3.4×10^{-6}
	96744.54	$J_K = 2_0 - 1_0 E$	5	20.1	3.4×10^{-6}
	96755.50	$J_K = 2_{+1} - 1_{+1} E$	5	28.0	2.6×10^{-6}

Notes. ^(a) Frequencies have been taken from Pickett et al. (1998) ^(b) Upper energy for methanol E -species includes the 7.9 K offset relative the $J_K = 0_0$ level of the A -species ^(c) A -coefficients from Müller et al. (2001)

Table 2. Observed comets with the OSO 20-m telescope

Comet	Observing UT date range	Int. time (hr)	R_h (au)	Δ (au)	d (km)
C/2016 U1 (NEOWISE)	2016-12-22 – 2017-01-10	14	0.71 – 0.34	0.75 – 1.07	5.2×10^4
45P/Honda-Mrkos-Pajdušáková	2017-01-18 – 2017-02-06	31	0.65 – 0.90	0.36 – 0.11	7.0×10^3
2P/Encke	2017-03-04 – 2017-03-17	15	0.37 – 0.38	0.75 – 0.68	4.1×10^4
41P/Tuttle-Giacobini-Kresák	2017-04-04 – 2017-04-24	170	1.05 – 1.06	0.14 – 0.17	8.7×10^3
C/2015 ER61 (PanSTARRS)	2017-04-06 – 2017-05-09	12	1.19 – 1.04	1.21 – 1.23	7.1×10^4
C/2017 E4 (Lovejoy)	2017-04-07	8	0.63	0.67	3.9×10^3
C/2015 V2 (Johnson)	2017-05-18 – 2017-05-19	13	1.67	0.87	5.0×10^4
C/2017 O1 (ASASSN1)	2017-10-12 – 2017-10-15	30	1.50	0.73 – 0.72	4.2×10^4
96P/Machholz	2017-10-30	5	0.16	1.04	6.0×10^4
46P/Wirtanen	2018-12-08 – 2019-01-18	232	1.06 – 1.16	0.096 – 0.22	4.7×10^3
C/2018 Y1 (Iwamoto)	2019-02-04 – 2019-02-19	38	1.29 – 1.30	0.46 – 0.39	2.4×10^4
2I/Borisov	2019-10-28 – 2019-11-18	89	2.21 – 2.06	2.66 – 2.18	1.4×10^5

Notes. Towards 96P/Machholz only CH₃OH was searched for. Both HCN and CH₃OH were observed in 46P/Wirtanen. For the rest of the comets only HCN was targeted.

January 2017 its heliocentric distance was 0.32 au. The spectrum presented in Fig. 1 is the average over 4 observing dates ranging from 22 December 2016 to 10 January 2017. It was not detected in HCN and the upper limit of the integrated intensity is listed in Table 3.

- 45P/Honda-Mrkos-Pajdušáková. This short-period comet discovered in 1948, hereafter called 45P, belongs to the Jupiter-family and has a period of 5.26 yr. The water production was estimated by Dello Russo et al. (2020) to be $(2 - 3) \times 10^{27} \text{ mol s}^{-1}$ using infrared spectroscopy in mid-February 2017. The same study reports an HCN production rate of $(3 - 4) \times 10^{24} \text{ mol s}^{-1}$. On 16 February 2017 there was also a CN outburst seen (Springmann et al. 2019). The HCN 1-0 triplet was not detected by us, see Fig. 1. The bulk of our HCN data was obtained early February 2017.
- 2P/Encke. This short-period comet was observed several times in the first half of March 2017. Our HCN observations resulted in a non-detection. Later in March, after perihelion, the water production rate was estimated to be $(3 - 4) \times 10^{28} \text{ mol s}^{-1}$ and the HCN production rate was $(3 - 6) \times 10^{25} \text{ mol s}^{-1}$ (Roth et al. 2018).
- 41P/Tuttle-Giacobini-Kresák. It was first observed in 1858 and later rediscovered in 1907 and 1952 as pointed out by Schleicher et al. (2019). Like 45P, this comet (hereafter called 41P) belongs to the Jupiter-family and has a period of 5.42 yr. In early April 2017 its peak water production

rate was $3.5 \times 10^{27} \text{ mol s}^{-1}$ (Moulane et al. 2018). The 41P nucleus rotation did undergo an unusually large slow-down with a rotation period increasing from 20 hr in March 2017 to more than 50 hr in early May (Schleicher et al. 2019). Our April 2017 HCN 1-0 detection, at the 4.6σ level, is shown in Fig. 1.

- C/2015 ER61 (PanSTARRS). This comet, hereafter ER61, follows a highly eccentric orbit and is suggested to originate in the inner Oort cloud (Meech et al. 2017). The OSO 20-m HCN 3.7σ detection is shown in Fig. 2. The spectrum is an average over three observing days in 2017; 6, 11, and 22 April. The observations took place after ER61 underwent an outburst on 4 April (Opitom et al. 2019). Sekanina (2017) suggests that the flare-up was caused by fragmentation of the nucleus creating a companion nucleus which was observed later in June. Our observations on 9 May were disregarded due to an inaccurate set of ephemeris. Saki et al. (2021) report a water production rate around $1 \times 10^{29} \text{ mol s}^{-1}$ in mid-April 2017 and an HCN rotational temperature near 70 K. This is consistent with the Atacama Large Millimeter/Submillimeter Array (ALMA) compact array HCN observations in mid-April by Roth et al. (2021b). Both studies determined the HCN production rate to be near $9 \times 10^{25} \text{ mol s}^{-1}$.
- C/2017 E4 (Lovejoy). This long-period comet (referred to as E4) appears to have originated in the inner Oort Cloud

(Faggi et al. 2018). Our observations took place on 7 April and resulted in an upper limit, see Fig. 2. Faggi et al. (2018) reported a water production rate of about 3×10^{28} mol s⁻¹ and an HCN production rate of about 5×10^{25} mol s⁻¹ only 3 days before our observations took place. The comet disintegrated in late April 2017.

- C/2015 V2 (Johnson). This Oort cloud comet (OCC), hereafter referred to as V2, follows a slightly hyperbolic orbit and was observed during one observing run stretching from 18-19 May in 2017 before the perihelion on 12 June. These observations resulted in an HCN 3.9σ detection, see Fig. 2. Combi et al. (2021) have estimated water production rates from SOHO/SWAN observations but no other direct molecular studies of V2 during this period of time have been found in the literature.
- C/2017 O1 (ASASSN1). This long-period comet, hereafter called O1, is a possible Manx comet (Brinkman 2020), i.e., a category of tail-less long-period comets which may have formed in the inner solar system and then been ejected to the outskirts. Our observation, resulting in a 7.4σ detection (Fig. 2), took place in two shifts in mid October 2017 (12/13 and 14/15).
- 96P/Machholz. This short-period comet has a rather peculiar high-inclination, low-perihelion orbit being a Jupiter family comet (JFC). Its nucleus is thought to be inactive (e.g. Eisner et al. 2019). Our observations, of CH₃OH only, were done when 96P/Machholz was at a heliocentric distance of 0.16 au on 30 October 2017 (the perihelion distance was 0.12 au for the 2017 apparition). Emission from CH₃OH was not detected with the OSO 20-m at this date, see Fig. 3, and the upper limit for the $J_K = 2_0 - 1_0 A^+$ line has been included in Table 5.
- 46P/Wirtanen. This JFC was the only comet in our sample that could be monitored in HCN, see Fig. 5 and Table 4. The first detection of HCN was made on 9 December 2018 and the last detection was made on 18 January 2019. The detection level was better than 3σ except on the dates 10 December and 10 January. On 20 December we detected the strongest HCN line intensity. The HCN spectrum of this date is shown in Fig. 4. Also CH₃OH was clearly detected, the spectrum (an average of data taken between 22 and 28 December) is shown in Fig. 6. Six different methanol lines around 96 GHz are seen (Table 5), each at a detection level of 5σ or better. It came very close to Earth in December 2018 (0.08 au) and was hence widely observed³. In addition, it showed much higher activity than during previous apparitions (Farnham et al. 2019). HCN was observed by Wang et al. (2020) ($J = 1 - 0$) and Coulson et al. (2020) ($J = 4 - 3$). The latter study also included $J = 7 - 6$ CH₃OH data. A week before closest approach to Earth, Roth et al. (2021c) observed the $J = 5 - 4$ CH₃OH lines using the ALMA array. They found variable CH₃OH outgassing consistent with the rotational period of 9 hrs (Farnham et al. 2021) of the nucleus. In December 2018 Biver et al. (2021) performed a molecular survey of 46P mainly using the Institut de RadioAstronomie Millimétrique (IRAM) 30-m telescope but also the Northern Extended Millimeter Array (NOEMA). At perihelion (12.9 December 2018) Moulane et al. (2019) reported a water production rate of 7.2×10^{27} mol s⁻¹ followed by a number of other infrared spectroscopy studies (Saki et al. 2020; Roth et al. 2021a; Bonev et al. 2021; Khan et al. 2021; McKay et al. 2021) as well as submillimetre observations of H₂¹⁸O (Lis et al. 2019).

Table 3. Observed HCN intensities and upper limits

Comet	Channel rms (mK)	I_{mb} (mK km s ⁻¹)
C/2016 U1 (NEOWISE)	7.5	< 11.2
45P/Honda-Mrkos-Pajdušáková	9.8	< 14.7
2P/Encke	12.9	< 19.4
41P/Tuttle-Giacobini-Kresák	3.8	23.8 ± 5.1
C/2015 ER61 (PanSTARRS)	10.0	49.3 ± 13.4
C/2017 E4 (Lovejoy)	17.3	< 23.2
C/2015 V2 (Johnson)	12.5	65.0 ± 16.7
C/2017 O1 (ASASSN1)	5.0	48.8 ± 6.6
C/2018 Y1 (Iwamoto)	5.5	68.2 ± 7.3
2I/Borisov	4.0	< 5.5

- C/2018 Y1 (Iwamoto). This bright and long-period comet, hereafter called Y1, came close (0.4 au) to Earth in February 2018. On February 5 DiSanti et al. (2019) report H₂O and HCN production rates of 2×10^{28} mol s⁻¹ and 4×10^{25} mol s⁻¹, respectively. By averaging data between 10 and 19 February we obtained a very clear 9σ detection of HCN, see Fig. 7. Data taken on February 4 were excluded in the analysis because of erroneous Doppler corrections.
- 2I/Borisov. Being only the second interstellar object known to have visited our Solar System, it was the first such object to show outgassing activity. This was confirmed already in September 2019 (Fitzsimmons et al. 2019). From interferometry imaging observations, using the ALMA (Cordiner et al. 2020), and Hubble Space Telescope (HST) observations (Bodewits et al. 2020), a CO production rate of about $(5 - 10) \times 10^{26}$ mol s⁻¹ around perihelion was found. Cordiner et al. (2020) also determined the HCN production rate to be 7×10^{23} mol s⁻¹. The 20-m observations in October and November 2018 only resulted, when averaging all data, in an upper limit of the HCN 1-0 emission, see Fig. 7.

In the case of 46P/Wirtanen (both HCN and CH₃OH) and C/2018 Y1 (Iwamoto) we see slightly shifted profiles in the sense that their peaks appear shifted with $\sim 0.3 - 0.4$ km s⁻¹ to lower velocities, see Figures 4, 6 and 7. This apparent blue-shift likely indicates that the gas outflow component directed towards Earth is more pronounced. Since both these comets were at $R_h > 1$ au at the time of observations, much of their sunward sides were then facing Earth. To illustrate this asymmetry more clearly a global average of all HCN high-resolution data for 46P/Wirtanen is also shown in Fig. 4 for which the blue peak is centered at -0.4 ± 0.1 km s⁻¹ when fitted with a Gaussian. The ratio of the blue to red wing emission for this spectrum is 2.6 ± 0.2 when using the velocity ranges $\pm(0.15 - 0.85)$ km s⁻¹ for the strongest $J_F = 1_2 - 0_1$ line. The observed line widths for 46P and Y1 seem to indicate an expansion velocity between 0.5 and 0.6 km s⁻¹.

4. Radiative transfer modelling of comets

As already mentioned, water is the main ingredient in the volatile material that is being outgassed from the comet surface. The gaseous material leaves the comet surface with a nearly constant expansion velocity v_e . Further out in the coma, the water molecules may be photo-ionized into H₂O⁺ and photo-dissociated mainly into OH and H (Rubin et al. 2009). Other molecules, like HCN, behave in a similar way. In addition, HCN is an important precursor to CN (Fray et al. 2005; Paganini et al. 2010) although heated CN-bearing dust could be a significant

³ https://wirtanen.astro.umd.edu/46P/46P_2018.shtml

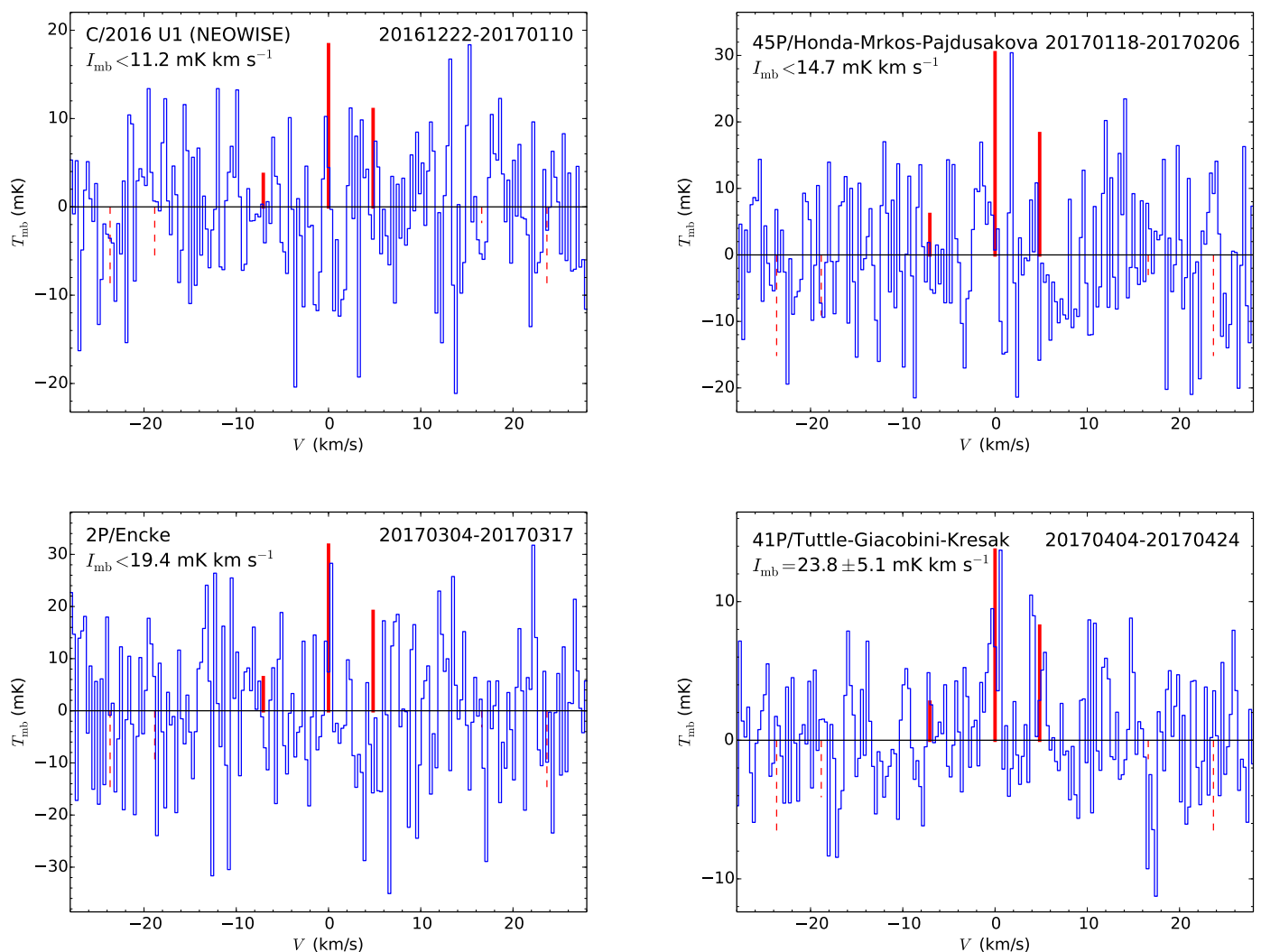


Fig. 1. OSO 20-m HCN 1-0 spectra towards the comets U1, 45P, 2P/Encke, and 41P. The velocity scale is in the reference frame of the comets and the intensity scale is in T_{mb} . The positions of the three hfs components are marked with red bars. The relative heights of the bars correspond to the statistical weights, g_u , in Table 1. Also the integrated intensity is shown together with 1σ error or as 1σ upper limit where applicable.

source to gaseous CN according to Hänni et al. (2020). This pure gas expansion may of course be modified when, for example, ions start to deflect when interacting with the Solar wind. This happens near what is called the contact surface, R_{CS} (Rubin et al. 2009). However, the radial distribution of neutral parent molecules (i.e. those with origin from the comet surface) is thought to follow the Haser relation (Haser 1957)

$$n_{\text{mol}}(r) = \frac{Q_{\text{mol}}}{4\pi r^2 v_e} \exp(-r\gamma_p/v_e), \quad (1)$$

as a function of cometocentric radius r , where Q_{mol} is the molecular production rate and γ_p is the photo-dissociation rate at the distance to the Sun.

4.1. Basic equations

As pointed out by Crovisier & Le Boulot (1983) the change rate of the physical conditions, like density decline due to expansion, in the cometary comae is not that different from the scale of molecular (in this case CO) radiative and collisional rates although their relative importance vary with radius. We here mainly follow the approach by Chin & Weaver (1984);

Bockelée-Morvan et al. (1984); Crovisier (1987); Bockelée-Morvan (1987) when setting up the basic equations governing the excitation.

For simplicity we start with a two-level system with upper level population n_u and lower level population n_l . The total population is $n = n_u + n_l$. The population change for the two levels can be expressed as the differential equations (DEs)

$$dn_u/dt = -n_u(A_{ul} + B_{ul}J_\nu + c_{ul} + \gamma_u) + n_l(B_{lu}J_\nu + c_{lu}) \quad (2)$$

$$dn_l/dt = +n_u(A_{ul} + B_{ul}J_\nu + c_{ul}) - n_l(B_{lu}J_\nu + c_{lu} + \gamma_l), \quad (3)$$

where A_{ul} is the spontaneous decay from u to l and $B_{ul}J_\nu$ and $B_{lu}J_\nu$ are the rates due to stimulated emission and absorption, respectively, when exposed to the averaged radiation field J_ν at the frequency ν . The downward and upward collisional rates are denoted c_{ul} and c_{lu} , respectively. These are the standard processes included for a two-level system. We have also added two other destruction rates referred to as γ_u and γ_l . These could, for example, represent destruction due to photo-dissociation or photo-ionization. We will hereafter assume that the destruction rate is equal for the upper and lower levels, that is, we set $\gamma = \gamma_u = \gamma_l$. By adding Eqs. (2) and (3), we then obtain

$$dn/dt = -\gamma n, \quad (4)$$

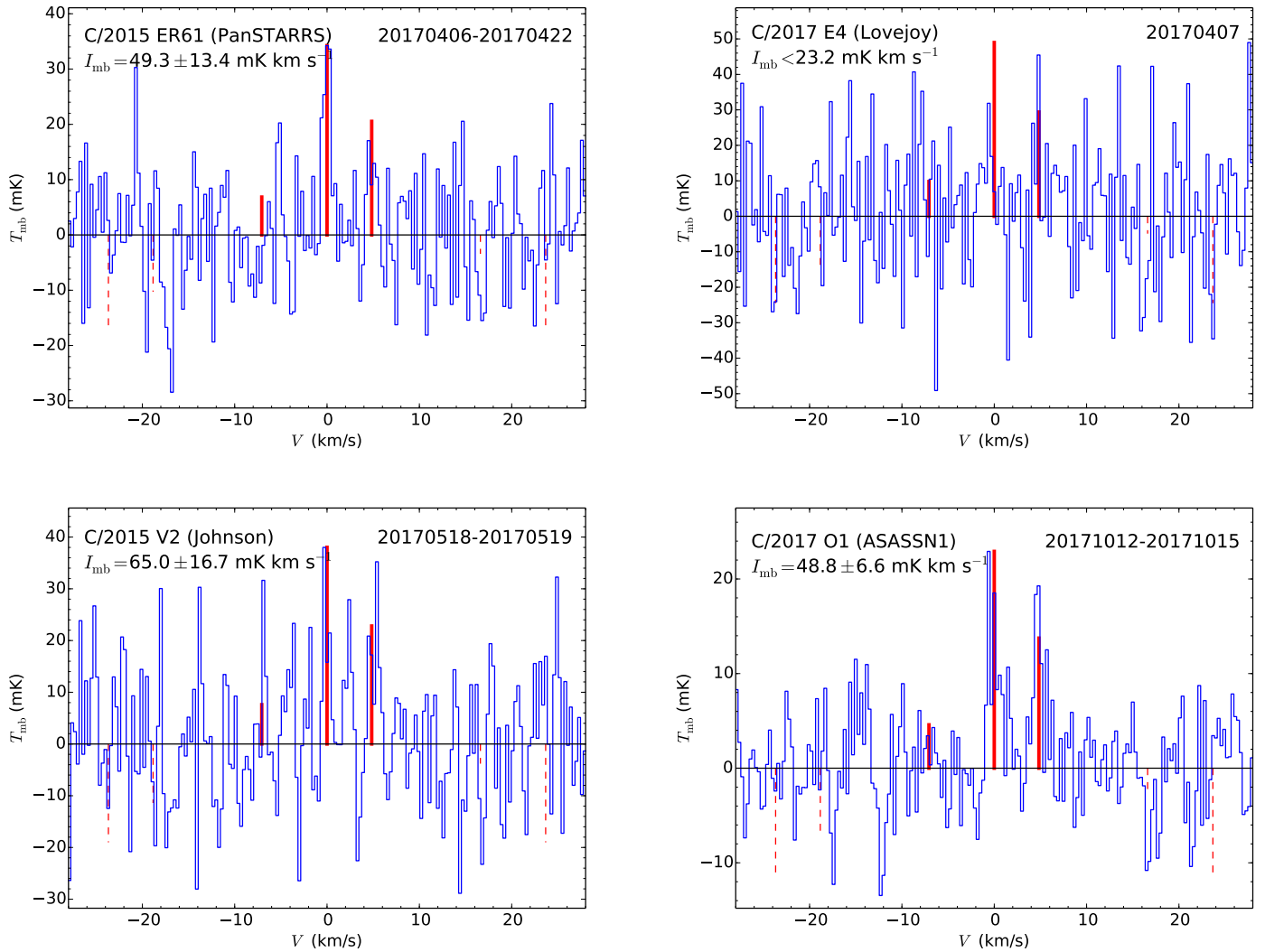


Fig. 2. HCN 1-0 spectra towards the comet ER61, E4, V2, and O1. Scales as in Fig. 1

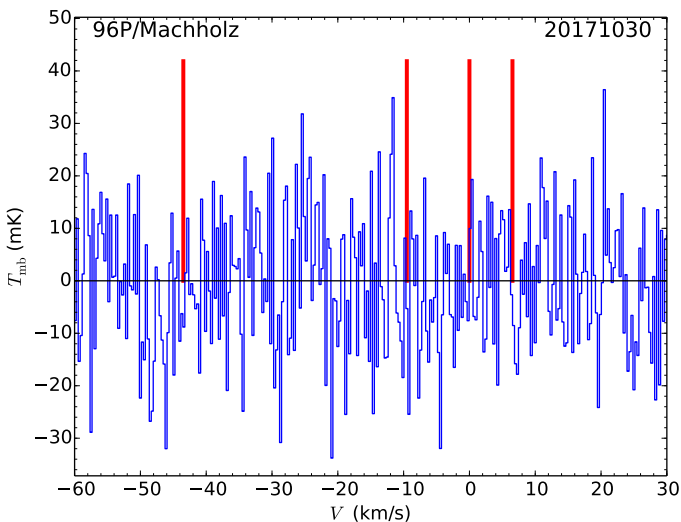


Fig. 3. CH₃OH spectrum towards the comet 96P/Machholz on 30 October 2017. The positions where the CH₃OH lines would appear are indicated by the red bars. Scales as in Fig. 1

which simply tells us that the total population $n(t)$ is exponentially decaying with time (if $\gamma > 0$).

In the case of a cometary coma, due to the outgassing, the molecules expand with a velocity according to v_e , which we here assume is constant. The cometocentric radius, r , is then given as $r = r_c + v_e t$ as a function of time. The radius of the comet nucleus is r_c . The destruction rate can then be modified to

$$\gamma = \gamma_p + \frac{2}{r} \frac{dr}{dt} = \gamma_p + \frac{2v_e}{r_c + v_e t}, \quad (5)$$

where γ_p is the destruction rate due to photo-dissociation (or photo-ionization) and the second term, $2v_e/r$, reflects the population dilution due to constant expansion. We note that the first part in Eq.(5) allows an expansion velocity varying with radius. However, we will hereafter always assume a constant gas expansion velocity. By changing dt to dr/v_e in Eqs. (2) and (3) it is straightforward to rewrite the population changes as a function of r instead of t . For instance, Eq. (4) then becomes

$$dn/dr = -(\gamma_p/v_e + 2/r)n, \quad (6)$$

which solves into the Haser distribution, Eq. (1), when integrated. Hence, by adopting this approach we can study possible time-dependent effects of the individual level populations n_u and n_l as function of cometocentric radius by solving the DEs in Eqs. (2) and (3) while still maintaining an overall decline due to the Haser equation. This may be of particular interest near

Table 4. 46P/Wirtanen HCN 2018/19 monitoring results

Date	MJD	R_h (au)	Δ (au)	I_{mb} mK km/s	$Q_{\text{HCN}}/10^{25}$ (mol/s)
1209	58461.8	1.056	0.088	135 ± 19	1.57 ± 0.21
1210	58462.1	1.056	0.086	144 ± 52	1.65 ± 0.60
1214	58466.7	1.056	0.078	135 ± 11	1.41 ± 0.11
1215	58467.5	1.056	0.078	108 ± 10	1.10 ± 0.10
1216	58468.5	1.056	0.077	78 ± 13	0.76 ± 0.12
1217	58469.1	1.057	0.078	88 ± 19	0.88 ± 0.18
1220	58472.7	1.060	0.081	145 ± 11	1.57 ± 0.12
1221	58473.5	1.062	0.083	101 ± 7	1.08 ± 0.07
1222	58474.2	1.063	0.085	84 ± 10	0.89 ± 0.10
1224	58476.8	1.067	0.091	85 ± 11	0.96 ± 0.12
1225	58477.5	1.069	0.095	96 ± 7	1.14 ± 0.08
1226	58478.5	1.071	0.098	77 ± 13	0.91 ± 0.15
1227	58479.2	1.074	0.102	110 ± 17	1.41 ± 0.21
1228	58480.8	1.076	0.106	77 ± 13	0.97 ± 0.16
1229	58481.5	1.079	0.111	115 ± 21	1.59 ± 0.28
1230	58482.5	1.082	0.115	75 ± 7	1.01 ± 0.09
1231	58483.5	1.085	0.120	104 ± 12	1.51 ± 0.17
0101	58484.5	1.088	0.125	73 ± 5	1.05 ± 0.07
0102	58485.2	1.091	0.130	65 ± 6	0.95 ± 0.07
0110	58493.7	1.123	0.173	40 ± 14	0.67 ± 0.23
0111	58494.2	1.128	0.179	44 ± 11	0.77 ± 0.19
0117	58500.8	1.158	0.215	50 ± 8	1.02 ± 0.16
0118	58501.2	1.164	0.222	28 ± 6	0.52 ± 0.11

Notes. Date is UT start of observation 2018/19mmdd. MJD corresponds to centre of time interval. See Sect. 4.2 for the HCN production rates.

Table 5. Observed CH₃OH intensities and upper limit

Comet	Line	I_{mb} mK km s ⁻¹
96P/Machholz	$J_K = 2_0 - 1_0 A^+$	< 10.7
46P/Wirtanen	$J_K = 2_0 - 1_0 A^+$	34.3 ± 2.7
	$J_K = 2_1 - 1_1 A^+$	20.0 ± 3.1
	$J_K = 8_0 - 7_1 A^+$	28.3 ± 2.7
	$J_K = 2_{-1} - 1_{-1} E$	19.6 ± 2.7
	$J_K = 2_0 - 1_0 E$	19.0 ± 2.7
	$J_K = 2_{+1} - 1_{+1} E$	13.4 ± 2.7

the contact surface (R_{CS}) where the electron properties vary very rapidly (they enter into the equations via c_{ul} and c_{lu}).

The above two-level system of equations is easily generalized into a multi-level system, but in order to simplify the solution of the DEs we here neglect the contribution from the line itself when calculating the averaged radiation field, \bar{J}_ν at any given radial point in the coma. We assume that the contributions to \bar{J}_ν only come from the diluted black body radiations of the comet nuclei, the Sun, and the 2.7 K cosmic background, respectively. Here we use the geometric dilution factors for the comet nuclei, $\beta_c(r)$, and that for the Sun, β_\odot . The remaining fraction of the 4π sky background is assumed to be filled by the $T_{cmb} = 2.7$ K cosmic background radiation. Neglecting effects due to shadowing, this can be expressed as

$$\bar{J}_\nu = \beta_c(r) J(T_c) + \beta_\odot J(T_\odot) + [1 - \beta_c(r) - \beta_\odot] J(T_{cmb}). \quad (7)$$

Here $J(T) = 1/(\exp(h\nu/kT) - 1)$ where h and k are Planck's and Boltzmann's constants, respectively. The radiation temperatures used are the surface temperature of the comet, T_c , and for the Sun we use $T_\odot = 5772$ K (Hertel & Schulz 2015). The geometric

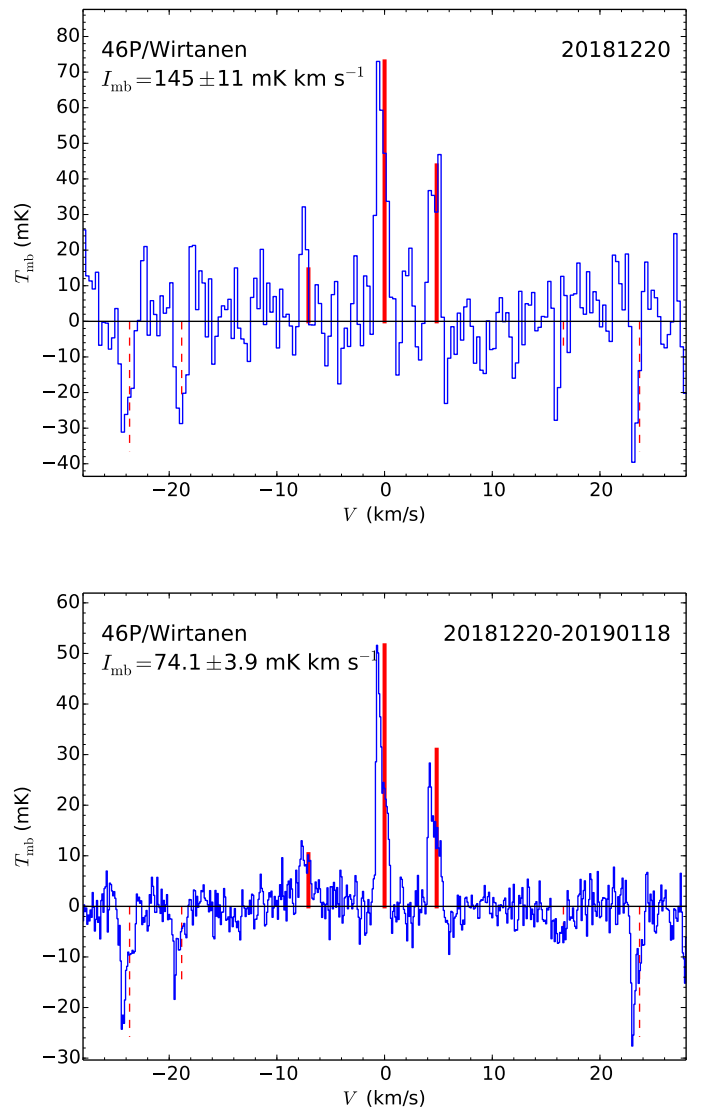


Fig. 4. Top: HCN 1-0 spectrum towards the comet 46P/Wirtanen on 20 December 2018. The positions, corresponding to a frequency throw of 7 MHz, of the negative artifacts of the HCN lines have been marked with negative dashed red lines. Bottom: Global average of all high-resolution (0.1 km s⁻¹) HCN data observed from 20 December 2018 to 18 January 2019. Scales as in Fig. 1.

dilution factor for the Sun, β_\odot , at 1 au is about 5×10^{-6} and at the surface of the comet we have that $\beta_c(r_c) = 1/2$. We have not included thermal radiation from dust particles in the modelling presented here.

In order to solve the DEs, Eqs. (2) and (3), we adopt initial population values, at $t = 0$ and $r = r_c$, appropriate to the production rate, $n(0) = Q/(4\pi r_c^2 v_e)$, and the initial excitation is entirely governed by the temperature of the comet surface, T_c . Following Bensch & Bergin (2004), we adopt a constant neutral gas kinetic temperature in the coma cloud set to the T_c value. We note that this is a simplification and some adiabatic cooling can take place (Biver et al. 2015). We use a fourth-order Runge-Kutta scheme (Abramowitz & Stegun 1972) when solving the DEs with adapting the step size because of the radial gradients. The coma model cloud is assumed to be spherically symmetric. At any radius, we can also determine level populations in the statistical equilibrium (SE) case similar to Paganini et al. (2010) by only including radiative and collisional processes.

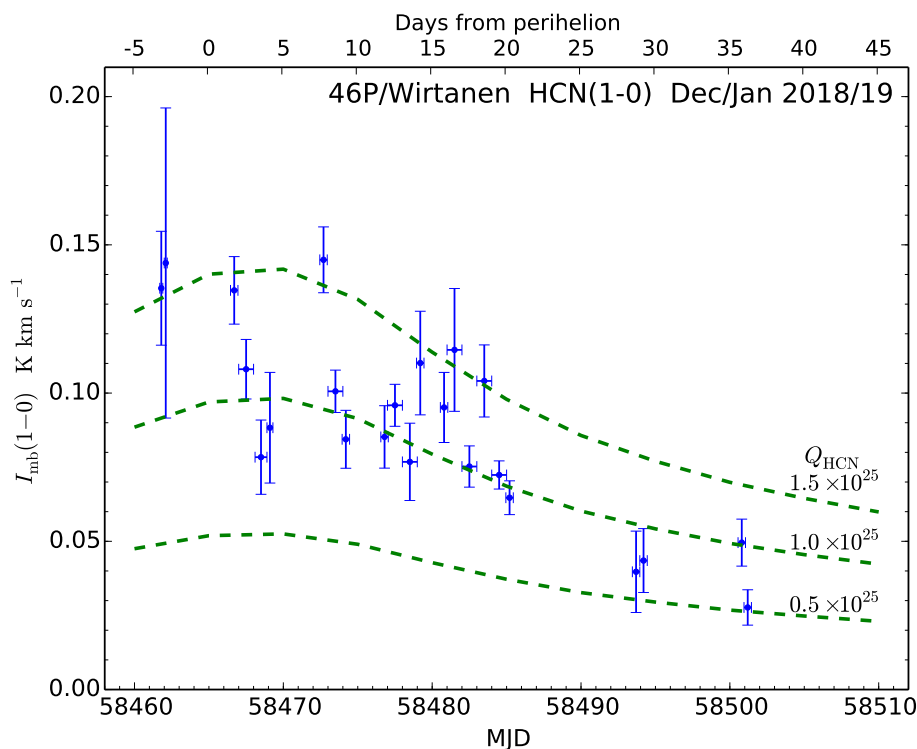


Fig. 5. OSO 20-m HCN 1-0 monitoring data towards 46P/Wirtanen in December 2018 and January 2019. The data points (blue marker with vertical 1σ errors bars, horizontal bars indicate range of observations), see Table 4, represent the integrated intensity as a function of modified Julian date (MJD) or days from perihelion. The dashed lines represent the results from the radiative transfer modelling, see Sect. 4, using 3 different HCN production rates from $0.5 \times 10^{25} \text{ mol s}^{-1}$ to $1.5 \times 10^{25} \text{ mol s}^{-1}$ as indicated for a temperature of 70 K and $Q_{\text{HCN}}/Q_{\text{H}_2\text{O}} = 0.1\%$.

We are only modelling HCN and CH_3OH comet emission in this study. The overall photo-dissociation and photo-ionization rates for HCN, CH_3OH and H_2O (given at 1 au from the quiet Sun) used come from the compilation by Huebner et al. (1992) which are essentially the same, for the molecules considered here, as those listed in the more recent work by Huebner & Mukherjee (2015). Depending on the heliocentric distance R_h of the comet, these are scaled by $(1/R_h)^2$. Furthermore, we assume R_h to be constant during the solution.

To properly account for collisional excitation we include collisions by electrons and H_2O molecules. While the molecule-electron collisions are relatively easy to determine, collisions by water molecules are much more difficult to compute. For instance, it is only very recently that collisional rate coefficients for the collision systems $\text{CO-H}_2\text{O}$ ($J \leq 10$) have been determined accurately (Faure et al. 2020). In the case of HCN (with hyperfine structure) and CH_3OH , no such calculations exist yet. Limited ($J < 8$) HCN- H_2O collisional rate coefficients have been determined by Dubernet & Quintas-Sánchez (2019) which are being used here together with the HCN-He rates of Dumouchel et al. (2010) for higher J ($J \geq 8$). The latter rates were scaled to approximately match the $J < 8$ HCN- H_2O rates before being concatenated to the Dubernet & Quintas-Sánchez (2019) rates. For CH_3OH we use the $\text{CH}_3\text{OH-H}_2$ rates of Rabli & Flower (2010) (for para H_2). We treat the methanol A - and E -species separately and do not include excited torsional states. The neutral collisional rates used are those valid for a kinetic temperature, T_k , of 50 K and then simply scaled with $(T_k/50 \text{ K})^{1/2}$ for other temperatures. We use the tabulated downward collisional rates and calculate the corresponding upward rates from detailed balance. For HCN-e collisional rates we adopt those determined by Faure et al. (2007) and for the electron excitation of CH_3OH we use a set of rates computed in the Born approximation.

Normally, to speed up the calculations, we only include energy levels below 150-250 K for HCN and CH_3OH . The exact cut-off depends on the temperature. However, we have the option to include higher energy levels for testing if there are any trun-

cation problems. Furthermore, also vibrationally excited levels (ν_2) for HCN can be fully included. However, the situation with a large number of levels together with levels with small populations requires much smaller step sizes to maintain the solution accuracy throughout the coma. This makes the computation very time consuming and a much faster way is to include effective pumping rates, see Paganini et al. (2010); Bensch & Bergin (2004), via the ν_1 , ν_2 , $2\nu_2$, and ν_3 vibrational states. We here only include the P - and R -branches for the ro-vibrational HCN transitions since they can cause redistribution of the ground state level populations in the outer coma (e.g. Bockelée-Morvan 1987). The Q -branch ($\Delta J = 0$) transitions do not do that by themselves (when neglecting rotational relaxations within the excited state). This way of incorporating effective pumping rates, adopting the radiation field in Eq. (7), is only valid when a small fraction of the molecules is in the excited states. This is typically the case for HCN (Bockelée-Morvan et al. 1984). We have not used any pumping rates for CH_3OH in our modelling here.

To fully quantify the collisional processes as a function of cometocentric radius, not only the collisional rates are needed but also the radial distributions of water molecules and electrons. The water distribution is assumed to follow the Haser equation (Eq. 1) assuming a water production rate $Q_{\text{H}_2\text{O}}$. The water production rate can be connected to the molecular (HCN or CH_3OH) production rate Q_{mol} via the abundance ratio $Q_{\text{mol}}/Q_{\text{H}_2\text{O}}$ normally referred to as the mixing ratio. To quantify the electron density radial distribution, $n_e(r)$, we adopt the approach by Bensch & Bergin (2004) who based their formulation on the work by Biver (1997) (see also Zakharov et al. 2007). These authors express $n_e(r)$ (and electron temperature) in terms of the water production rate and like Paganini et al. (2010) we use $x_{n_e} = 0.3$ as the density scaling factor. The rather complex radial behaviour of the electron density and temperature is visualized by Bensch & Bergin (2004) in their Fig. 1.

The solution of the time-dependent radiative transfer is in practice accomplished by a Python code called `comrad.py`. This code is adapted to read molecular data files used in the Lei-

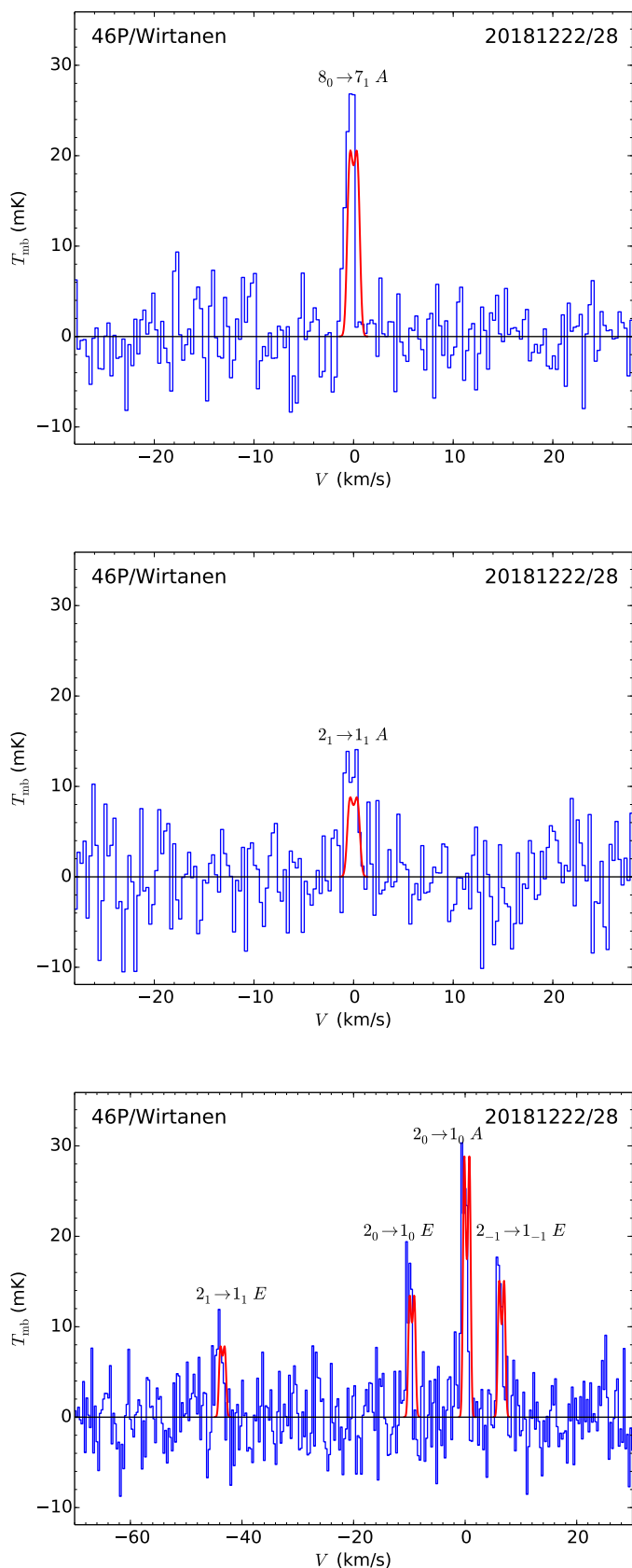


Fig. 6. OSO 20-m methanol spectra towards 46P/Wirtanen when averaging data between 22 and 28 December 2018. The red spectra represent the modelling results of the radiative transfer modelling, see Sect. 4, using a CH₃OH production rate of 1.6×10^{26} mol s⁻¹ and a kinetic temperature of 70 K.

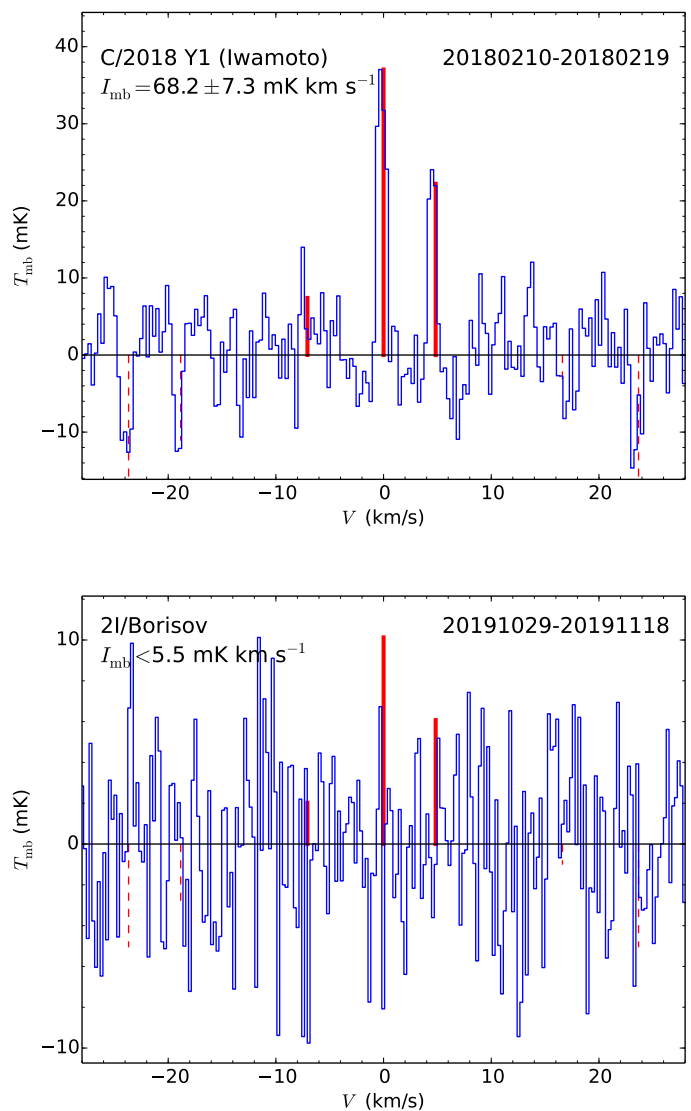


Fig. 7. Top: OSO 20-m HCN 1-0 spectrum towards C/2018 Y1 (Iwamoto). It is an average of data between 10 and 19 February 2019. Bottom: The HCN spectrum observed towards 2I/Borisov in October/November 2019. Scales as in Fig. 1.

den atomic and molecular database (Schöier et al. 2005) slightly modified to also include photo-destruction values in the Solar radiation field at 1 au (Huebner et al. 1992) and a section of IR pumping transitions (for HCN *P*- and *R*-branches between the ground state and the excited states ν_1 , ν_2 , $2\nu_2$, and ν_3). The frequencies and *A*-coefficients of the IR pumping transitions have been taken from the HITRAN molecular database (Gordon et al. 2017). After the molecular level populations have been determined as a function of cometocentric radius, we obtain the modelled spectra, assuming a constant expansion velocity and a turbulent velocity width, by convolving the projected radial intensity distribution with a gaussian appropriate to the telescope beam size and the comet distance (Δ). Although the HCN level populations are strongly affected in the outer coma by the IR pumping transitions, the impact on the resulting line intensities of ground state rotational transitions is small since the major contribution comes from regions of high density (this can be pronounced by smaller observing beams).

In Appendix A we will investigate the effects of the time-dependent radiative transfer calculations by comparing the re-

sults to those of steady-state SE calculations. We will use the time-dependent radiative transfer model described above in the analysis of our HCN and CH₃OH data and the results of the modelling are described in the following section.

4.2. Model results

Our HCN modelling results are summarized in Table 6. Here also the properties used for each comet (46P/Wirtanen only 20 December 2018) are listed. The adopted nucleus radius, r_c , which serves as a starting point for the model calculation, is also included but has essentially no impact on the modelling results. For 46P and Y1 we have obtained the expansion velocities from the line widths. This results in 0.55 km s^{-1} for both comets. Coulson et al. (2020) found a similar value of $\sim 0.6 \text{ km s}^{-1}$ for 46P (at $R_h = 1.06 \text{ au}$). We note that, for 45P, Lovell et al. (2017) report an outflow velocity of about 0.8 km s^{-1} from OH observations (at $R_h = 0.54 \text{ au}$). Biver et al. (2006) determined a relation of v_e and heliocentric distance (in au): $v_e \sim 0.8 / \sqrt{R_h} \text{ km s}^{-1}$. This relation yields expansion velocities near 1.3 km s^{-1} for 2P/Encke and around 0.55 km s^{-1} for 2I/Borisov. The observed v_e around 0.55 km s^{-1} for 46P and Y1 lie below this relation. For 46P and Y1 the above relation predicts 0.76 km s^{-1} and 0.70 km s^{-1} , respectively. However, for the other comets we have used an expansion velocity according to this relation.

In the case of U1 and O1 we have not found representative water production rates in the literature. Here we instead used the mean value of $Q_{\text{HCN}}/Q_{\text{H}_2\text{O}} = 0.1\%$ from Bockelée-Morvan & Biver (2017) to determine an appropriate $Q_{\text{H}_2\text{O}}$ for the modelling. It should be noted that the derived Q_{HCN} does not depend strongly on the adopted $Q_{\text{H}_2\text{O}}$ (as verified below by the 46P results where a factor of two increase in $Q_{\text{H}_2\text{O}}$ resulted in a 7% increase in the required Q_{HCN}).

When possible we also use published values for the gas temperature (which also is used for the neutral gas kinetic temperature here and T_e out to R_{CS}) as indicated in the table. The kinetic temperature is clearly dependent on the heliocentric distance R_h and Biver et al. (1997) estimated the kinetic temperature of C/1995 O1 (Hale-Bopp) from CH₃OH (and CO) observations as a function of R_h to be around 100 K at 1 au and approximately scaling as R_h^{-1} with heliocentric distance. In the case of 46P/Wirtanen we use our CH₃OH observations to estimate the kinetic temperature, see below. If a kinetic temperature estimate is lacking, we used 60 K for comets with $R_h \geq 1.3 \text{ au}$ and 70 K for the remaining comets in the model calculations. These values approximately reflect the temperature behaviour as a function of heliocentric distance found by Biver et al. (1999) for C/1992 B2 (Hyakutake) or by DiSanti et al. (2016) in the case of D/2012 S1 (ISON). The temperature estimates used in Table 6 sometimes stem from rotational temperatures of molecules like H₂O or CH₃OH. How well this rotational temperature reflects the gas kinetic temperature of the major collision agent (H₂O) depends on the degree of thermalization. Also, collisions by electrons may change the excitation of the molecular probe (Xie & Mumma 1992).

Due to the observed blue-shifted line profiles for 46P/Wirtanen and also C/2018 Y1 (Iwamoto) it is likely that there is an anisotropic distribution of Q_{HCN} in the sense that the production rate is higher on comet sunward side than on the anti-sunward side (with a factor of 2-3 difference, see Fig. 4). This was also noted by Wang et al. (2020) and Biver et al. (2021) for HCN and for CH₃OH by Roth et al. (2021c). Our modelled values, based on a spherically symmetric model geometry, thus refer to an average production rate.

As already mentioned, in the case of 46P/Wirtanen we can estimate the gas kinetic temperature since we have detected lines with quite different upper energies (as high as 83 K). Another aspect of CH₃OH transitions, due to the nuclear spin directions of the methyl group H atoms, is that they come in two different symmetry species, *A* and *E*, which are, as pointed out by Bockelée-Morvan et al. (1994), radiatively and collisionally uncoupled apart from possible line overlaps. The lowest *E*-state is about 8 K above the lowest *A*-state. Depending on the formation mechanism they may be produced in unequal amounts. This can be the case at low temperatures (e.g. Wirström et al. 2011). If the temperature appropriate for methanol formation in comets is larger than 8 K, then we expect the production rates of the *A*- and *E*-species of CH₃OH to be equal. We have performed a grid testing with temperatures ranging from 40 K to 120 K (in steps of 10 K) and $Q_{\text{CH}_3\text{OH}}$ from $1.0 \times 10^{26} \text{ mol s}^{-1}$ to $3.0 \times 10^{26} \text{ mol s}^{-1}$ (in steps of $0.1 \times 10^{26} \text{ mol s}^{-1}$). The water production rate used was $Q_{\text{H}_2\text{O}} = 1.0 \times 10^{28} \text{ mol s}^{-1}$ which is an average of the $Q_{\text{H}_2\text{O}}$ determined by (Combi et al. 2020) for the dates 22-28 December 2018. The grid combination of kinetic temperature and $Q_{\text{H}_2\text{O}}$ that gave the best fit (as indicated by smallest χ^2 -value) to the observed integrated intensities in Table 5 was for a temperature of $70 \pm 15 \text{ K}$ and $Q_{\text{CH}_3\text{OH}} = (1.6 \pm 0.1) \times 10^{26} \text{ mol s}^{-1}$ or 1.6% of the water production rate.

The fitting indicated, within the errors, also that the CH₃OH *A*- and *E*-species are being outgassed in equal amounts in 46P/Wirtanen. The resulting model spectra are shown in Fig. 6 together with the observed spectra.

As noted above, the CH₃OH modelling of 46P/Wirtanen resulted in a kinetic temperature of 70 K. Using this temperature and $Q_{\text{H}_2\text{O}} = 1.6 \times 10^{28} \text{ mol s}^{-1}$ which is the 22 December value of Combi et al. (2020), we find that for the 20 December data an HCN production rate of $(1.6 \pm 0.1) \times 10^{25} \text{ mol s}^{-1}$ is matching the observed integrated intensity, see Tables 6 and 4. Using a fixed value for the ratio $Q_{\text{HCN}}/Q_{\text{H}_2\text{O}}$ of 0.1%, as found for the 20 December data, we have run models for 3 different HCN production rates at different dates and entered the expected 1-0 integrated intensity in Fig. 5. The production rates are $(0.5, 1.0, 1.5) \times 10^{25} \text{ mol s}^{-1}$ which encompass most of the observed line intensities. Also included in Table 6 is the HCN production rate when adopting a lower water production rate as indicated by the infrared spectroscopy results (e.g. Bonev et al. 2021) a few days prior to 20 December. The change in Q_{HCN} is less than 10%. The individual HCN production rates, see Table 4, are shown in Fig. 8 together with the water production rates obtained using SOHO/SWAN by Combi et al. (2020). These results will be discussed in the next section.

Our CH₃OH observations of 96P/Machholz only resulted in an upper limit, see Table 5. Adopting $T_c = 90 \text{ K}$ and $Q_{\text{CH}_3\text{OH}}/Q_{\text{H}_2\text{O}} = 1\%$ this upper limit corresponds to a very high methanol production rate. We estimate the upper limit production rate to be above $10^{28} \text{ mol s}^{-1}$. The poor constraining of $Q_{\text{CH}_3\text{OH}}$ is due to the fact that 96P was only at $R_h = 0.12 \text{ au}$ at the time of the measurements and the size of the neutral coma is considerably smaller due to the effective destruction of H₂O and CH₃OH molecules near the Sun.

5. Discussion

We will in this section first discuss the previously determined HCN production rates as well as the upper limits. We will also discuss the HCN production rates as an indirect indicator of water production rates via mixing ratios. In the case of

Table 6. Properties of the comets and results of the HCN modelling

Comet	R_h (au)	Δ (au)	r_c (km)	v_e (km/s)	T_c (K)	Q_{H_2O} (mol/s)	Q_{HCN} (mol/s)	Q_{HCN}/Q_{H_2O} (%)
C/2016 U1 (NEOWISE)	0.50	0.90	1.0	1.1	70	...	$< 7.8 \times 10^{25}$...
45P/Honda-Mrkos-Pajdušáková	0.88	0.12	0.4 ^(a)	0.8	70	$2 \times 10^{27(b)}$	$< 3.2 \times 10^{24}$	< 0.16
2P/Encke	0.38	0.70	2.2 ^(c)	1.3	70 ^(d)	$3 \times 10^{28(d)}$	$< 2.2 \times 10^{26}$	< 0.7
41P/Tuttle-Giacobini-Kresák	1.05	0.15	0.6 ^(e)	0.8	70	$3.5 \times 10^{27(f)}$	$(4.5 \pm 1.0) \times 10^{24}$	0.13 ± 0.03
C/2015 ER61 (PanSTARRS)	1.10	1.22	0.94 ^(c)	0.7	70 ^(g)	$1 \times 10^{29(g)}$	$(8.2 \pm 2.1) \times 10^{25}$	0.082 ± 0.021
C/2017 E4 (Lovejoy)	0.63	0.67	1.0	1.0	70	$3 \times 10^{28(h)}$	$< 6.3 \times 10^{25}$	< 0.21
C/2015 V2 (Johnson)	1.67	0.87	1.7 ^(c)	0.6	60	$4 \times 10^{28(i)}$	$(3.5 \pm 0.9) \times 10^{25}$	0.088 ± 0.022
46P/Wirtanen (2018-12-20)	1.06	0.08	0.7 ^(j)	0.55	70 ^(k)	$1.6 \times 10^{28(j)}$ $8 \times 10^{27(l)}$	$(1.6 \pm 0.1) \times 10^{25}$ $(1.5 \pm 0.1) \times 10^{25}$	0.10 ± 0.01 0.19 ± 0.02
C/2017 O1 (ASASSN1)	1.50	0.72	0.92 ^(c)	0.6	60	...	$(2.2 \pm 0.2) \times 10^{25}$...
C/2018 Y1 (Iwamoto)	1.30	0.42	1.0	0.55	60	$2.1 \times 10^{28(m)}$	$(2.2 \pm 0.2) \times 10^{25}$	0.10 ± 0.02
2I/Borisov	2.10	2.40	1.0	0.55	50 ⁽ⁿ⁾	$6.5 \times 10^{26(n)}$	$< 6.3 \times 10^{24}$	< 1.0

Notes. ^(a) From Combi et al. (2019). ^(b) From Dello Russo et al. (2020). ^(c) Comet radius from Paradowski (2020). ^(d) From Roth et al. (2018). ^(e) See Howell et al. (2017) and Boehnhardt et al. (2020). ^(f) April 2017 average from Moulane et al. (2018). ^(g) Adapted from Saki et al. (2021). ^(h) From Faggi et al. (2018). ⁽ⁱ⁾ From Combi et al. (2021). ^(j) Adapted from Combi et al. (2020). ^(k) Estimated from the CH₃OH data in this paper. ^(l) Based on IR spectroscopy data (Bonev et al. 2021). See also Lis et al. (2019). ^(m) Preliminary data by DiSanti et al. (2019). ⁽ⁿ⁾ Adapted from Cordiner et al. (2020).

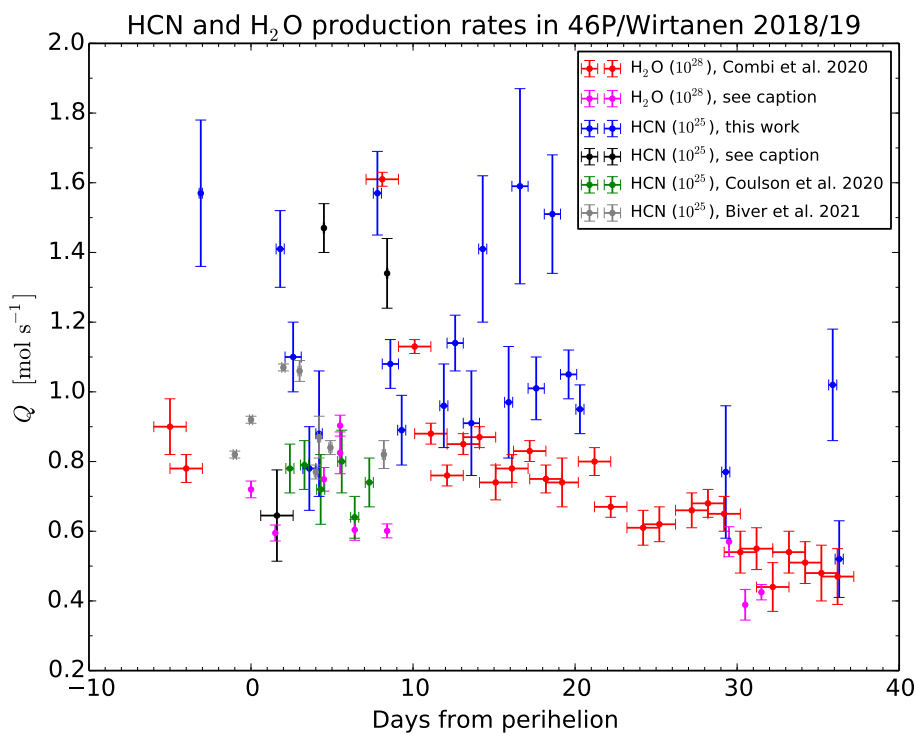


Fig. 8. HCN and H₂O production rates in 46P/Wirtanen as a function of days from perihelion (12.9 December 2018 UT). The HCN rates (blue) have been determined from the intensities (only those detected above the 3 σ level) in Table 4. The water production rates (red) contemporary with our Q_{HCN} results, are from Combi et al. (2020). The perihelion value of Q_{H_2O} from Moulane et al. (2019) and the post-perihelion values from Saki et al. (2020) (14 and 19 December), Roth et al. (2021a) (18 December), Bonev et al. (2021) (17/18 December), Khan et al. (2021) (21 December), and McKay et al. (2021) (11–13 January) are included (magenta). Also, with black markers, the Q_{HCN} as estimated by Wang et al. (2020) (14/15 December), Bonev et al. (2021) (17 December) and Khan et al. (2021) (21 December) are shown. The HCN observations by Coulson et al. (2020) have been included using green markers and those from Biver et al. (2021) are shown with grey markers. The lengths of the error bars in the vertical direction relate to the 1 σ uncertainties in the rates while the in horizontal direction they reflect the time length over which they refer to. As indicated, the HCN rates should be scaled by 10^{25} and the water rates by 10^{28} .

46P/Wirtanen, the monitoring results can be used to see variations in the HCN production rates on time scales of 1 day and these will be compared to other observations of HCN and H₂O production rates. Our usage of methanol as a thermal probe will also be discussed. Finally, our time-dependent treatment of the radiative transfer of comets will be discussed in relation to a more standard approach performed in the steady-state limit of the SE assumption.

5.1. HCN production rates

As can be seen in Table 6 we have detected HCN in 2 JFCs (41P and 46P, the latter comet is discussed in more detail in the next

section) and 4 long-period OCCs (ER61, V2, O1, and Y1). For the 6 comets with HCN detections, the determined HCN production rates fall in the range $(0.5 - 8) \times 10^{25}$ mol s⁻¹ and there is no obvious difference between the two type of comets. For the 5 comets where we also have independent (and reasonably contemporary) water production rates, the HCN to H₂O mixing ratios are in the range 0.08-0.13%. This range of mixing ratios is consistent with the values as determined from radio observations and discussed by Mumma & Charnley (2011) and by Bockelée-Morvan & Biver (2017). However it is smaller, by a factor of about 2, than the typical value in Dello Russo et al. (2016). The latter study, based on high-resolution infrared spectroscopy, compiles a typical range of mixing ratios of 0.15-0.27%. Our ratios, near 0.1% for 41P, ER61, V2, 46P, and Y1, are outside this

range but are well above the lower extreme value of 0.03% found by Dello Russo et al. (2016).

In the case of 41P our HCN data were obtained over a longer period in April 2017. The average water production rate, derived from OH observations by Moulane et al. (2018) over this period, is estimated to be about $3.5 \times 10^{27} \text{ mol s}^{-1}$ with no larger variations. Moulane et al. (2018) also report CN production rates in the range $(4 - 5) \times 10^{24} \text{ mol s}^{-1}$ which is similar to our HCN production rate of $(4.5 \pm 1.0) \times 10^{24} \text{ mol s}^{-1}$. This could indicate that the CN radicals observed in 41P mainly stem from photodissociation of HCN. However, given the uncertainties and that our Q_{HCN} is an average (over time and over the coma) one cannot exclude a contribution to Q_{CN} from dust grains as suggested by Dello Russo et al. (2016) and Hänni et al. (2020).

The ER61 observations (HCN and H_2O) by Saki et al. (2021) occurred on three occasions in our 6-22 April observation range and we here adopt an average of their water production rates of $1 \times 10^{29} \text{ mol s}^{-1}$. They deduced HCN mixing ratios in the range 0.11-0.14% somewhat higher than our value of 0.082%. This is possibly a result of that our HCN data reflect a larger time span. However, the ALMA results (Roth et al. 2021b) indicate an HCN mixing ratio (0.072%) consistent with our value.

For Y1, the used water production rate of DiSanti et al. (2019) dates from about a week before our estimate of the HCN production rate. Adopting this $Q_{\text{H}_2\text{O}}$, the mixing ratio is $0.10 \pm 0.02 \%$. DiSanti et al. (2019) obtain an HCN mixing ratio of 0.2% on 4 February 2018. This could indicate variations in $Q_{\text{H}_2\text{O}}$ if we assume that the HCN production rate is constant over this period of observations.

In the case of the remaining HCN detections, V2 and O1, no other directly determined molecular production rates have been found to date in the literature. However, for V2, Combi et al. (2021) estimated the water production rate, using SOHO/SWAN observations, to about $4 \times 10^{28} \text{ mol s}^{-1}$ near our observation date. The corresponding mixing ratio is about 0.08%. We also note that Venkataramani & Ganesh (2018) reported on the absence of molecular emissions towards V2 at $R_h = 2.83 \text{ au}$ but they noted that such emissions appeared later on a low level when $R_h = 2.3 \text{ au}$. Our 3.9σ detection was made at $R_h = 1.67 \text{ au}$.

In 5 of our observed comets (U1, 45P, 2P/Encke, E4, and 2I/Borisov), we only obtained upper limits on Q_{HCN} , see Table 6. At the time of writing, no molecular observational results for U1 have been reported in the literature so here we have nothing to compare to. The HCN production rate of $(3 - 4) \times 10^{24} \text{ mol s}^{-1}$ in 45P found by Dello Russo et al. (2020) refers to dates in mid February 2017. Our non-detection, $Q_{\text{HCN}} < 3.2 \times 10^{24} \text{ mol s}^{-1}$, is from early February and indicates that the production rate of HCN was about same or lower in early February. Roth et al. (2018) observed HCN in 2P/Encke, after perihelion, on 21 and 25 March, resulting in $Q_{\text{HCN}} \sim (3 - 6) \times 10^{25} \text{ mol s}^{-1}$. Our upper limit only indicates that Q_{HCN} , before and around perihelion, did not exceed 6-8 times this value. For E4, Faggi et al. (2018) determined an HCN production rate of $5 \times 10^{25} \text{ mol s}^{-1}$. This was 3 days before we obtained an upper limit of $6 \times 10^{25} \text{ mol s}^{-1}$ so apparently there was no significant increase in Q_{HCN} from April 4 to 7. Our upper limit on Q_{HCN} towards 2I/Borisov is consistent with the ALMA HCN detection on 14/15 December by Cordiner et al. (2020). They determined that $Q_{\text{HCN}} = 7 \times 10^{23} \text{ mol s}^{-1}$.

Taken together, the HCN mixing ratios, based on our $J = 1 - 0$ data, seem to fall near 0.1% when we have reasonably contemporary estimates of $Q_{\text{H}_2\text{O}}$.

5.2. Variation in the HCN production rates for 46P/Wirtanen

We determined HCN production rates for 46P/Wirtanen (Table 4) from a few days before perihelion until 36 days after perihelion, see Figs. 5 and 8. There are clear variations in Q_{HCN} , sometimes on a daily basis, but it is also evident that Q_{HCN} has decreased by a factor of 2-3 some month after the perihelion passage. We note that Wang et al. (2020) observed HCN 1-0 on 14-15 December and obtained a Q_{HCN} (based on LTE calculations) of about half our value and that the IRAM 30-m observations (Biver et al. 2021) on 14 December result in a Q_{HCN} in between our value ($1.4 \times 10^{25} \text{ mol s}^{-1}$) and that of Wang et al. (2020). A few days later, in the range 15-17 December, the IRAM 30-m data show Q_{HCN} determinations very close to our values. The James Clerk Maxwell Telescope (JCMT) HCN(4-3) data of Coulson et al. (2020) showed little daily variation in Q_{HCN} in the period 15 December to the early UT hours of 20 December. The HCN production rates determined by Wang et al. (2020), Biver et al. (2021) and Coulson et al. (2020) are all included in Fig. 8. The HCN(4-3) Q_{HCN} results agree quite well with our results up until 20 December. Here we see a clear increase in Q_{HCN} to $(1.6 \pm 0.1) \times 10^{25} \text{ mol s}^{-1}$, by a factor of two over that from Coulson et al. (2020). However, the JCMT observations relate to the early UT hours and our observations are from about 12 hrs later the same day. This would indicate an outburst event during the day of 20 December. However, early on 21 December the zero-spacing NOEMA observations of Biver et al. (2021) again indicates a lower Q_{HCN} of $0.8 \times 10^{25} \text{ mol s}^{-1}$ so if there was an outburst it must have been rather short ($\lesssim 12 \text{ hr}$) not to be recorded by the NOEMA observations. In fact, similar changes of $Q_{\text{CH}_3\text{OH}}$, by about a factor 2, was seen by Roth et al. (2021c) connecting it to the rotation period time scale of 9 hrs.

Based on infrared spectroscopy, Bonev et al. (2021) reported an HCN production rate of $(1.47 \pm 0.07) \times 10^{25} \text{ mol s}^{-1}$ on 17 December. This Q_{HCN} is significantly higher than our value of $(0.9 \pm 0.2) \times 10^{25} \text{ mol s}^{-1}$ and the value, $(0.7 \pm 0.1) \times 10^{25} \text{ mol s}^{-1}$, of Coulson et al. (2020) from the same date. Four days later, on 21 December, Khan et al. (2021) observed HCN also by infrared spectroscopy. Their HCN production rate averaged to about $1.3 \times 10^{25} \text{ mol s}^{-1}$ which is near our value, see Table 4, $1.1 \times 10^{25} \text{ mol s}^{-1}$ on the same date. The Q_{HCN} values from Bonev et al. (2021) and Khan et al. (2021) have been included in Fig. 8.

As already pointed out in Sect. 4.2, there appears to be a clear difference, a factor of 2-3, in the outgassing activity on the sunward vs anti-sunward parts of the comet nucleus over the course of about one month. As reported by Biver et al. (2015) based on their water line observations by the Microwave Instrument for the Rosetta Orbiter (MIRO) of the JFC 67P/Churyumov-Gerasimenko, the nightside water production rate was low, $< 1\%$ of the dayside production rate (at $r_h = 3.4 \text{ au}$). Later, at $r_h = 1.8 \text{ au}$, Fink et al. (2016) report for 67P that about 17% of the total water production emerges from the nightside. In any case, this is a higher day-to-nightside activity ratio than we see for 46P but our ratio is averaged over a period of a month in which the daytime fraction as seen by our telescope beam changed (elongation varied from 160 to 140 deg from 20 December 2018 to 18 January 2019).

The SOHO/SWAN monitoring observations (Combi et al. 2020) to estimate $Q_{\text{H}_2\text{O}}$ in 46P coincide partly in time with our observations and provide estimates of the water production rate variation. Since these results are based on Ly- α observations of the hydrogen coma (dissociation product from H_2O and OH), they refer to an average water production of the 2-3 days prior to the actual observation date (as indicated by the horizontal error

bars in Fig. 8) so the $Q_{\text{H}_2\text{O}}$ determined this way may not probe activity variations on shorter time scales. However, the trend we see in Q_{HCN} from 20 December until 18 January (8 to 36 days after perihelion) is consistent with a mixing ratio near 0.1%. For the week preceding this time span, Biver et al. (2021) report essentially the same value $0.11 \pm 0.01\%$. There are a few Q_{HCN} estimates in our monitoring time span 8–36 days after perihelion that seem to indicate an HCN mixing ratio near 0.2%. This is also the case for the pre-perihelion observations. To distinguish whether this reflects real changes in the mixing ratio, by a factor of about 2, or is an effect of different time-averaging would need $Q_{\text{H}_2\text{O}}$ measurements with ~ 1 day time-resolution or better. If it is an effect of time-averaging, the HCN production rate will be a good indicator of the water production rate in the case of 46P/Wirtanen. The increase in Q_{HCN} seen by us on 20 December seems supported by the large water production rate reported by Combi et al. (2020) 2–3 days later and, as discussed earlier, the Q_{HCN} reported by Khan et al. (2021) on 21 December but not by the NOEMA observations early UT hours on 21 December.

5.3. Coma gas kinetic temperature and methanol production in 46P/Wirtanen

In Sect. 4.2, we determined the gas kinetic temperature of 46P, from methanol data taken over the time span 22–28 December, to be 70 ± 15 K. Furthermore, the deduced production rate of $Q_{\text{CH}_3\text{OH}} = (1.6 \pm 0.1) \times 10^{26} \text{ mol s}^{-1}$ corresponds to a methanol mixing ratio of about 1.6%. Our mixing ratio is very near the JFC average value of 1.7% as compiled by Dello Russo et al. (2016) and slightly less than the JFC median value of about 2% as compiled by Mumma & Charnley (2011).

Most other methanol observations of 46P refer to the period around or the week after the perihelion. For instance, on 7–9 December Roth et al. (2021c) used ALMA observations to determine methanol rotation temperatures in the range from 50 K to 80 K. Biver et al. (2021) determined, using IRAM 30-m CH₃OH observations, 6-day averages (over the range 12–18 December) of the gas temperature in the range 53–75 K. On 16 December Coulson et al. (2020) used the JCMT to observe three methanol lines around 338 GHz. They determined the rotation temperature to $T_{\text{rot}} \sim 30 - 50$ K. Using infrared spectroscopy observations on 18 December, Roth et al. (2021a) report a methanol rotation temperature of about 90 K. In addition, Biver et al. (2021) also made a single methanol observation on 25.8 December 2018 UT, within our observing time range, which resulted in a gas temperature of 43 ± 7 K.

Three studies estimate H₂O rotation temperatures of 46P. On 14 and 19 December, Saki et al. (2020) determined the water rotation temperature to be about 85 K. On 18 December, Roth et al. (2021a) report a rotation temperature of about 90 K. Later, on 21 December Khan et al. (2021) derived temperatures of 80 K to 90 K. Our derived value of the gas kinetic temperature of about 70 K, as averaged over 22–28 December, is consistent with the studies mentioned above. There is a possibility that the temperature has decreased from 80–90 K to about 40–50 K during our observations (cf. Khan et al. 2021; Biver et al. 2021). However, this notion is somewhat complicated by the variation of temperature estimates (30–90 K) prior to our observations.

In the case of the methanol production in 46P, we begin with noting that on 7–9 December, the ALMA CH₃OH observations (Roth et al. 2021c) resulted in varying CH₃OH production rates in the range $(2.0 - 3.6) \times 10^{26} \text{ mol s}^{-1}$. The IRAM 30-m data by Biver et al. (2021) determined $Q_{\text{CH}_3\text{OH}}$, averaged

over 12–18 December, to $(2.6 \pm 0.2) \times 10^{26} \text{ mol s}^{-1}$. The JCMT observations on 16 December (Coulson et al. 2020) resulted in $(3.5 \pm 0.2) \times 10^{26} \text{ mol s}^{-1}$. On 18 December, Roth et al. (2021a) report a methanol production rate around $2 \times 10^{26} \text{ mol s}^{-1}$. A few days later, on 21 December, Khan et al. (2021) reported a similar methanol production rate of $2.5 \times 10^{26} \text{ mol s}^{-1}$. These estimates of $Q_{\text{CH}_3\text{OH}}$ are all higher than our later, 22–28 December, value of $Q_{\text{CH}_3\text{OH}} = (1.6 \pm 0.1) \times 10^{26} \text{ mol s}^{-1}$. The NOEMA observations (Biver et al. 2021) on 25.8 December 2018 UT resulted in $(1.84 \pm 0.14) \times 10^{26} \text{ mol s}^{-1}$ close to our value.

As noted above, we adopt $Q_{\text{H}_2\text{O}} = 1.0 \times 10^{28} \text{ mol s}^{-1}$ which is an average of the $Q_{\text{H}_2\text{O}}$ determined by (Combi et al. 2020) for the dates 22–28 December 2018. This $Q_{\text{H}_2\text{O}}$ results in a mixing ratio of 1.6%. For the 2 week period prior to our methanol observations, mixing ratios in the range 2–5% have been reported (Roth et al. 2021c; Biver et al. 2021; Coulson et al. 2020; Roth et al. 2021a; Khan et al. 2021). Based on this, we suggest that the average methanol mixing ratio decreased by about a factor two from around perihelion into our observing period of 22–28 December.

The production rates of the methanol *A*- and *E*-species are about equal for 46P within the uncertainties. This would point at ≥ 8 K temperature environment during the formation of the methanol molecules. Finally, the determined kinetic temperature is related to the used CH₃OH-H₂O collisional rate coefficients which in our case were based on the CH₃OH-H₂ rates. As already pointed out, accurate collisional rate coefficients currently only exist for the collision systems CO-H₂O (Faure et al. 2020) and HCN-H₂O (Dubernet & Quintas-Sánchez 2019).

5.4. Time-dependent radiative transfer versus SE calculations

To study time-dependent effects, we used fragment B of 73P as test case (see Appendix A) and we noted that HCN level population deviations relative steady-state SE-calculations were of the order 5–15% for $J = 0$ to 5. The water production rate for 73P/B is around $2 \times 10^{28} \text{ mol s}^{-1}$. We also found that the time-dependent deviations would be relatively larger for comets with lower water production rates since the collisions with water molecules will be less frequent in the inner part of the coma. Likewise, by reducing the effect of electron-HCN collisions the time-dependent effects became more pronounced. For molecules with lower electric dipole moments (and hence generally lower *A*-coefficients), we expect the effects to be more pronounced - at least in the outer coma where radiative processes dominate (see Fig. A.1). However, strong IR-pumping could counteract the effect in the outer coma making the details of the excitation picture very complicated. We expect that the influence of time-dependent effects on the HCN level populations will be small ($\lesssim 20\%$) for $Q_{\text{H}_2\text{O}} \geq 10^{28} \text{ mol s}^{-1}$.

It is worth pointing out that the total molecular population is bound to follow the radial Haser distribution so that molecular production rates based on the analysis of a larger number of transitions should be less affected by the time-dependent effects encountered here.

Also, the present modelling work neglects excitation effects at a certain position in the coma caused by line radiation from other parts of the coma (same as assuming optically thin radiation in the level population determination). This may be a good approximation for most cometary molecular probes but an important exception is water excitation (e.g. Bockelée-Morvan 1987; Bensch & Bergin 2004). Extending our model into using

an escape probability formalism (cf. Gersch & A’Hearn 2014) is a possibility but would need an iterative solution technique. That is; solving for the entire coma using an initial guess (using the DE here or simply an SE solution), include the line radiation in Eq. (7), and then repeat the procedure with time-dependent solutions throughout the coma until the level populations converge. Presumably, this would be a very time consuming technique but could be tried for water excitation in comets. Solution methods based on the Monte Carlo technique (Bernes 1979) or those using accelerated lambda iteration (Rybicki & Hummer 1991; Bergman & Humphreys 2020) appear to be less suitable for time-dependent studies since they rely on the SE steady state assumption. However, in the escape probability formalism (e.g. Bockelée-Morvan 1987; van der Tak et al. 2007; Zakharov et al. 2007), the A -coefficients are replaced by βA where β is the (local) escape probability for the transition in question. In the case of optically thick transitions ($\beta \sim 1/\tau$) this could imply that time-dependent effects, due a reduction in radiative excitation, could be of a relatively higher importance.

Another aspect is that because the radiative transfer formulation here is in the time domain, it would be easier to incorporate chemical and photolytic state-to-state reactions when solving excitation of several molecules at the same time in the coma. Finally, it is worth stressing that most radiative transfer models, including the one presented here, assume a spherically symmetric coma geometry. Remote observations and in-situ studies of cometary comae clearly show deviations from this geometry and models like that of Debout et al. (2016) could be used for studying time-dependent effects also in anisotropic comae.

6. Summary and conclusions

We performed spectral line observations of HCN and CH₃OH transitions towards a sample of bright comets using the OSO 20-m telescope. From the observations, we determined molecular production rates using a radiative transfer model taking into account time-dependent effects. Our main conclusions are:

- We detected HCN(1-0) in 6 comets, 2 JFCs and 4 OCCs, of our sample. For 5 of these comets we could determine the HCN mixing ratio using published values of $Q_{\text{H}_2\text{O}}$. The determined HCN mixing ratios were all near 0.1% (0.08-0.013%).
- We detected HCN emission in 46P/Wirtanen on 21 occasions from 9 December 2018 to 18 January 2019. When comparing with contemporary $Q_{\text{H}_2\text{O}}$ determinations we find a typical mixing ratio near 0.1% with possible variations up to 0.2%. This variation can also be due to short-time activity variations ($\lesssim 1$ d) not reflected in the Ly- α observations used for determining $Q_{\text{H}_2\text{O}}$. We also noted a clear asymmetry in the observed HCN and CH₃OH line profiles in the sense that the sunward activity was about a factor of 2-3 as strong as the outgassing activity on the 46P night-side.
- In addition to HCN, we detected 6 CH₃OH transitions in 46P/Wirtanen around two weeks after perihelion in December 2018. This enabled us to determine the gas kinetic temperature to be about 70 K. The methanol mixing ratio was found to be 1.6% about half that of the methanol mixing ratio during the 2 weeks prior to our observations.
- To interpret our HCN and CH₃OH observations, we used a radiative transfer code in which we allowed for time-dependent effects on the level populations by relaxing the normal steady-state assumption of statistical equilibrium (SE) in the cometary coma. In our test case (73P fragment B, see

Fig. A.2) we noticed 5-15% deviations of the HCN level populations as compared to SE values. We recognized that the time-dependent effects may be more pronounced for comets with lower water production rates and if the molecular excitation via electron collisions becomes less efficient. For $Q_{\text{H}_2\text{O}} \gtrsim 10^{28}$ mol s⁻¹ the time-dependent effects in the HCN excitation should be small.

Acknowledgements. We are very grateful to L. Paganini for sharing his HCN modelling details. We also thank N. Biver for making his 1997 thesis available to us. The Onsala Space Observatory national research infrastructure is funded through Swedish Research Council grant No 2017-00648.

References

- Abramowitz, M. & Stegun, I. A. 1972, Handbook of Mathematical Functions (Dover, New York)
- Belitsky, V., Lapkin, I., Fredrixon, M., et al. 2015, A&A, 580, A29
- Bensch, F. & Bergin, E. A. 2004, ApJ, 615, 531
- Bergman, P. & Humphreys, E. M. L. 2020, A&A, 638, A19
- Bernes, C. 1979, A&A, 73, 67
- Biver, N. 1997, PhD thesis, Université Paris 7
- Biver, N., Bockelée-Morvan, D., Boissier, J., et al. 2021, A&A, 648, A49
- Biver, N., Bockelée-Morvan, D., Colom, P., et al. 1997, Earth Moon and Planets, 78, 5
- Biver, N., Bockelée-Morvan, D., Crovisier, J., et al. 1999, AJ, 118, 1850
- Biver, N., Bockelée-Morvan, D., Crovisier, J., et al. 2006, A&A, 449, 1255
- Biver, N., Hofstadter, M., Gulkis, S., et al. 2015, A&A, 583, A3
- Bockelée-Morvan, D. 1987, A&A, 181, 169
- Bockelée-Morvan, D. & Biver, N. 2017, Philosophical Transactions of the Royal Society of London Series A, 375, 20160252
- Bockelée-Morvan, D., Crovisier, J., Baudry, A., et al. 1984, A&A, 141, 411
- Bockelée-Morvan, D., Crovisier, J., Colom, P., & Despois, D. 1994, A&A, 287, 647
- Bodewits, D., Noonan, J. W., Feldman, P. D., et al. 2020, Nature Astronomy, 4, 867
- Boehnhardt, H., Riffeser, A., Ries, C., Schmidt, M., & Hopp, U. 2020, A&A, 638, A8
- Bonev, B. P., Dello Russo, N., DiSanti, M. A., et al. 2021, The Planetary Science Journal, 2, 45
- Bonev, B. P., Mumma, M. J., DiSanti, M. A., et al. 2006, ApJ, 653, 774
- Brinkman, C. L. 2020, in American Astronomical Society Meeting Abstracts, American Astronomical Society Meeting Abstracts, 454.02
- Chin, G. & Weaver, H. A. 1984, ApJ, 285, 858
- Combi, M. R., Bertaux, J. L., Quémerais, E., Ferron, S., & Mäkinen, J. T. T. 2011, ApJ, 734, L6
- Combi, M. R., Mäkinen, T., Bertaux, J. L., et al. 2020, The Planetary Science Journal, 1, 72
- Combi, M. R., Mäkinen, T. T., Bertaux, J. L., Quémerais, E., & Ferron, S. 2019, Icarus, 317, 610
- Combi, M. R., Shou, Y., Mäkinen, T., et al. 2021, Icarus, 365, 114509
- Cordiner, M. A., Milam, S. N., Biver, N., et al. 2020, Nature Astronomy, 4, 861
- Coulson, I. M., Liu, F.-C., Cordiner, M. A., et al. 2020, AJ, 160, 182
- Crovisier, J. 1987, A&AS, 68, 223

- Crovisier, J. & Le Boulrot, J. 1983, *A&A*, 123, 61
- Debout, V., Bockelée-Morvan, D., & Zakharov, V. 2016, *Icarus*, 265, 110
- Dello Russo, N., Kawakita, H., Bonev, B. P., et al. 2020, *Icarus*, 335, 113411
- Dello Russo, N., Kawakita, H., Vervack, R. J., & Weaver, H. A. 2016, *Icarus*, 278, 301
- Despois, D., Gerard, E., Crovisier, J., & Kazes, I. 1981, *A&A*, 99, 320
- DiSanti, M., Saki, M., Gibb, E., et al. 2019, in *EPSC-DPS Joint Meeting 2019*, Vol. 2019, EPSC–DPS2019–822
- DiSanti, M. A., Bonev, B. P., Gibb, E. L., et al. 2016, *ApJ*, 820, 34
- Dubernet, M. L. & Quintas-Sánchez, E. 2019, *Molecular Astrophysics*, 16, 100046
- Dumouchel, F., Faure, A., & Lique, F. 2010, *MNRAS*, 406, 2488
- Eisner, N. L., Knight, M. M., Snodgrass, C., et al. 2019, *AJ*, 157, 186
- Faggi, S., Villanueva, G. L., Mumma, M. J., & Paganini, L. 2018, *AJ*, 156, 68
- Farnham, T. L., Kelley, M. S. P., Knight, M. M., & Feaga, L. M. 2019, *ApJ*, 886, L24
- Farnham, T. L., Knight, M. M., Schleicher, D. G., et al. 2021, *The Planetary Science Journal*, 2, 7
- Faure, A., Lique, F., & Loreau, J. 2020, *MNRAS*, 493, 776
- Faure, A., Varambhia, H. N., Stoecklin, T., & Tennyson, J. 2007, *MNRAS*, 382, 840
- Fink, U., Doose, L., Rinaldi, G., et al. 2016, *Icarus*, 277, 78
- Fitzsimmons, A., Hainaut, O., Meech, K. J., et al. 2019, *ApJ*, 885, L9
- Fray, N., Bénilan, Y., Cottin, H., Gazeau, M. C., & Crovisier, J. 2005, *Planet. Space Sci.*, 53, 1243
- Gersch, A. M. & A’Hearn, M. F. 2014, *ApJ*, 787, 36
- Giorgini, J. D., Yeomans, D. K., Chamberlin, A. B., et al. 1996, in *AAS/Division for Planetary Sciences Meeting Abstracts #28*, AAS/Division for Planetary Sciences Meeting Abstracts, 25.04
- Gordon, I. E., Rothman, L. S., Hill, C., et al. 2017, *J. Quant. Spectr. Rad. Transf.*, 203, 3
- Hänni, N., Altwegg, K., Pestoni, B., et al. 2020, *MNRAS*, 498, 2239
- Haser, L. 1957, *Bulletin de la Societe Royale des Sciences de Liege*, 43, 740
- Hertel, I. V. & Schulz, C.-P. 2015, *Atoms, Molecules and Optical Physics 2* (Springer, Berlin, Heidelberg)
- Howell, E. S., Lejoly, C., Taylor, P. A., et al. 2017, in *AAS/Division for Planetary Sciences Meeting Abstracts #49*, AAS/Division for Planetary Sciences Meeting Abstracts, 414.24
- Huebner, W. F., Keady, J. J., & Lyon, S. P. 1992, *Ap&SS*, 195, 1
- Huebner, W. F. & Mukherjee, J. 2015, *Planet. Space Sci.*, 106, 11
- Ip, W. H. 1985, *Advances in Space Research*, 5, 233
- Khan, Y., Gibb, E. L., Bonev, B. P., et al. 2021, *The Planetary Science Journal*, 2, 20
- Läuter, M., Kramer, T., Rubin, M., & Altwegg, K. 2020, *MNRAS*
- Lecacheux, A., Biver, N., Crovisier, J., et al. 2003, *A&A*, 402, L55
- Lis, D. C., Biver, N., Bockelée-Morvan, D., et al. 2013, *ApJ*, 774, L3
- Lis, D. C., Bockelée-Morvan, D., Boissier, J., et al. 2008, *ApJ*, 675, 931
- Lis, D. C., Bockelée-Morvan, D., Güsten, R., et al. 2019, *A&A*, 625, L5
- Lovell, A. J., Amason, C., Howell, E. S., et al. 2017, in *AAS/Division for Planetary Sciences Meeting Abstracts #49*, AAS/Division for Planetary Sciences Meeting Abstracts, 420.04
- McKay, A. J., DiSanti, M. A., Cochran, A. L., et al. 2021, *The Planetary Science Journal*, 2, 21
- Meech, K. J., Schambeau, C. A., Sorli, K., et al. 2017, *AJ*, 153, 206
- Moulane, Y., Jehin, E., José Pozuelos, F., et al. 2019, in *EPSC-DPS Joint Meeting 2019*, Vol. 2019, EPSC–DPS2019–1036
- Moulane, Y., Jehin, E., Opitom, C., et al. 2018, *A&A*, 619, A156
- Müller, H. S. P., Thorwirth, S., Roth, D. A., & Winnewisser, G. 2001, *A&A*, 370, L49
- Mumma, M. J. & Charnley, S. B. 2011, *ARA&A*, 49, 471
- Mumma, M. J., DiSanti, M. A., Dello Russo, N., et al. 2003, *Advances in Space Research*, 31, 2563
- Opitom, C., Yang, B., Selman, F., & Reyes, C. 2019, *A&A*, 628, A128
- Paganini, L., Villanueva, G. L., Lara, L. M., et al. 2010, *ApJ*, 715, 1258
- Paradowski, M. L. 2020, *MNRAS*, 492, 4175
- Pickett, H. M., Poynter, R. L., Cohen, E. A., et al. 1998, *J. Quant. Spectr. Rad. Transf.*, 60, 883
- Rabli, D. & Flower, D. R. 2010, *MNRAS*, 406, 95
- Roth, N. X., Bonev, B. P., DiSanti, M. A., et al. 2021a, *The Planetary Science Journal*, 2, 54
- Roth, N. X., Gibb, E. L., Bonev, B. P., et al. 2018, *AJ*, 156, 251
- Roth, N. X., Milam, S. N., Cordiner, M. A., et al. 2021b, *ApJ*, 921, 14
- Roth, N. X., Milam, S. N., Cordiner, M. A., et al. 2021c, *The Planetary Science Journal*, 2, 55
- Rubin, M., Altwegg, K., Balsiger, H., et al. 2019, *MNRAS*, 489, 594
- Rubin, M., Hansen, K. C., Gombosi, T. I., et al. 2009, *Icarus*, 199, 505
- Rybicki, G. B. & Hummer, D. G. 1991, *A&A*, 245, 171
- Saki, M., Gibb, E. L., Bonev, B. P., et al. 2020, *AJ*, 160, 184
- Saki, M., Gibb, E. L., Bonev, B. P., et al. 2021, *AJ*, 162, 145
- Schleicher, D. G., Knight, M. M., Eisner, N. L., & Thirouin, A. 2019, *AJ*, 157, 108
- Schöier, F. L., van der Tak, F. F. S., van Dishoeck, E. F., & Black, J. H. 2005, *A&A*, 432, 369
- Sekanina, Z. 2017, *arXiv e-prints*, arXiv:1712.03197
- Springmann, A., Harris, W., Ryan, E., & Lejoly, C. 2019, in *EPSC-DPS Joint Meeting 2019*, Vol. 2019, EPSC–DPS2019–1904
- van der Tak, F. F. S., Black, J. H., Schöier, F. L., Jansen, D. J., & van Dishoeck, E. F. 2007, *A&A*, 468, 627
- Venkataramani, K. & Ganesh, S. 2018, in *European Planetary Science Congress*, EPSC2018–1220
- Wang, Z., Zhang, S.-B., Tseng, W.-L., et al. 2020, *AJ*, 159, 240
- Wirström, E. S., Geppert, W. D., Hjalmarsen, Å., et al. 2011, *A&A*, 533, A24
- Wirström, E. S., Lerner, M. S., Källström, P., et al. 2016, *A&A*, 588, A72
- Xie, X. & Mumma, M. J. 1992, *ApJ*, 386, 720
- Zakharov, V., Bockelée-Morvan, D., Biver, N., Crovisier, J., & Lecacheux, A. 2007, *A&A*, 473, 303

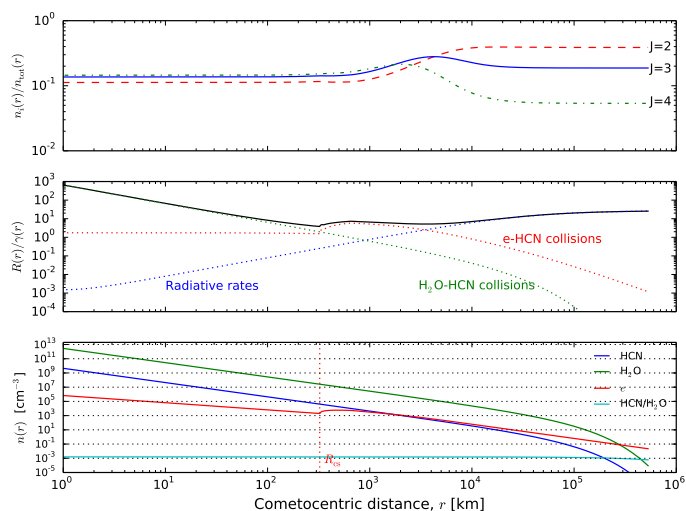


Fig. A.1. Time dependent HCN modelling with parameters corresponding to the fragment B of 73P/Schwassmann-Wachmann. The upper plot shows the fractional level populations for levels $J = 2, 3, 4$ as a function of cometocentric distance. The middle plot shows the relative importance of different downward rates for the HCN $J = 3 - 2$ transition. As indicated, the included rates are radiative (excluding IR pumping rates), and collisional rates both for electrons and water molecules. The sum of these rates is included as a black line. They are normalized with the time dependent rate due to destruction and constant expansion, see Eq. (5). The bottom panel depicts the radial density variations. The blue curve is the total HCN density and the green curve represents the water density behaviour. The electron density, $n_e(r)$, is drawn in red. Also the HCN/ H_2O ratio is shown. It is not entirely flat since when the photo-dissociation becomes important in the outer coma, HCN and H_2O molecules are destroyed with slightly different rates.

Appendix A: Validation of the time-dependent model

As a starting point for the validation of our time-dependent model described in Sect. 4, we adopt the case for comet 73P/Schwassmann-Wachmann, hereafter 73P, which broke into fragments during its 2006 apparition. Paganini et al. (2010) observed the HCN $J = 3 - 2$ and $J = 4 - 3$ lines in 73P on May 12 2006 using the Heinrich Hertz Submillimeter Telescope (HHSMT). Contemporary Caltech Submillimeter Observatory (CSO) HCN observations of 73P/B were also made (Lis et al. 2008). Paganini et al. (2010) also performed comprehensive modelling of the HCN emission to which we can compare our modelling results. We adopt the values for fragment B these authors used: $Q_{\text{HCN}} = 3 \times 10^{25} \text{ mol s}^{-1}$, $Q_{\text{H}_2\text{O}} = 1.9 \times 10^{28} \text{ mol s}^{-1}$, $T = 90 \text{ K}$, and $v_e = 0.53 \text{ km s}^{-1}$. To further mimic their setup we neglect hfs and include effective pumping rates. In the upper panel of Fig. A.1 we show the HCN fractional level populations for $J = 2, 3, 4$ as a function of cometocentric radius.

The appearance of the level population variation looks very similar to that of Fig. 1 in Paganini et al. (2010) hinting at any time-dependent effects not being huge in this particular case. Our late time values are about a factor 1.2-1.5 larger than those of Paganini et al. (2010). The middle panel in this figure depicts the relative importance of the different HCN excitation mechanisms (for $J = 3 - 2$). In the inner coma, collisions with water molecules are most important while in the outer coma, radiative processes dominate. It between, as shown by Xie & Mumma (1992), collisions by electrons are the most important excitation mechanism.

The different downward rates in the middle panel of Fig. A.1 have been normalized with the rate due to expansion and destruc-

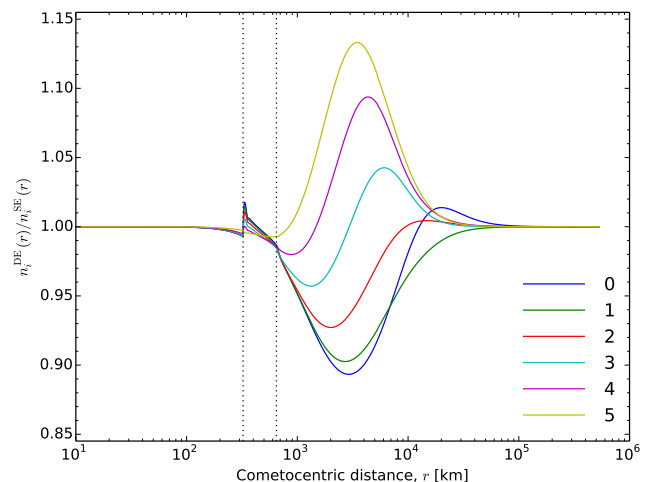


Fig. A.2. The HCN level ($J = 0$ to 5) population variation as a function of cometocentric radius, for the time-dependent modelling (see Fig. A.1) adopting the parameters for fragment B of 73P/Schwassmann-Wachmann during its 2006 passage. The level populations have been normalized to their SE-values to visualize time-dependent effects. The vertical dotted lines correspond to radii R_{CS} and $2R_{\text{CS}}$ between which the electron temperature increases from 90 K to 10^4 K.

tion, γ in Eq. (5). When this ratio is around 1 or smaller, we may see time dependency effects. As visualized in the bottom panel of Fig. A.1, where the radial density variations of water, HCN and electrons are shown, the electron properties change very rapidly at the contact surface radius, $R_{\text{CS}} = 324 \text{ km}$. Here the electron temperature T_e rises very steeply from the comet temperature to around 10^4 K (Ip 1985; Bensch & Bergin 2004) accompanied with an increase of the electron density.

It is around a cometocentric radius near R_{CS} , see the middle panel in Fig. A.1, where we should start to see the time-dependent effects on the excitation (cf. Chin & Weaver 1984). To investigate this in more detail, we display in Fig. A.2 the ratio of the time dependent level populations ($J = 0$ to 5) to those valid in the SE-limit. The level population ratios are very close to 1 up to about $r = 100 \text{ km}$ (cf. Bockelée-Morvan et al. 1984) and from radii larger than about $r = (4 - 5) \times 10^4 \text{ km}$. After the sharp increase in T_e from 90 K to 10^4 K over the interval $[R_{\text{CS}}, 2R_{\text{CS}}]$ the level populations deviate from the SE-values during the settling – in this case at most up to 7% for $J = 2$. The low- J level populations settle a little later than do the high- J level populations since their A -coefficients are smaller. This deviation is not directly related to the change in electron properties but to that of the normalized rates, middle panel in Fig. A.1, which are close to 1. Due to its large electric dipole moment, HCN rotational transitions have large A -coefficients and we expect that for molecules with smaller spontaneous rates (eg. CO) the settling of the level populations will take place further out in the coma. The deviations from the SE populations will be larger if $Q_{\text{H}_2\text{O}}$ is reduced since HCN- H_2O collisions will be less effective in settling the populations. For instance, using $Q_{\text{H}_2\text{O}} = 1 \times 10^{28} \text{ mol s}^{-1}$ in our test case, the time-dependent $J = 2$ population deviations reach 9% and for $Q_{\text{H}_2\text{O}} = 4 \times 10^{28} \text{ mol s}^{-1}$ they are at the 5% level. By reducing the amount of electron collisions (by lowering x_{n_e} from 0.3 to 0.15) the effects are less clear. Firstly, the initial time-dependent deviation at R_{CS} will be less pronounced but the settling at larger radii, $10^3 - 10^4 \text{ km}$, will show larger deviations. Increasing the amount of electron collisions will reduce the slower time-dependent behaviour (and, of course, increase the deviation at R_{CS}).